 https://doi.org/10.3311/PPch.42701

Periodica Polytechnica Chemical Engineering, 70(1), pp. 64–87, 2026

The Interplay between Dopant and the Surface Structure of an Electron Transport Layer in N719 Solid State Dye-Sensitized Solar Cells: An Analysis of Aluminum-doped Faceted TiO_2 with Mg-$CuCrO_2$ Transport Channels Using the SCAPS-1D Framework

Eli Danladi[1,2*], Lehlohonolo F. Koao[3], Macdenis O. Egbuhuzor[4], Tshwafo E. Motaung[5], Setumo V. Motloung[6]

[1] Department of Mathematical and Physical Sciences, Faculty of Engineering, Built Environment and Information Technology, Central University of Technology, Free State, Private Bag X20539, 9300 Bloemfontein, Republic of South Africa
[2] Department of Physics, Faculty of Science, Federal University of Health Sciences, P. M. B. 145, Otukpo, Benue State, Nigeria
[3] Department of Physics, Faculty of Natural and Agricultural Sciences, University of the Free State, Qwaqwa Campus, Private Bag X 13, 9866 Phuthaditjhaba, Republic of South Africa
[4] Department of Metallurgical and Materials Engineering, Faculty of Engineering, University of Nigeria, 410001 Nsukka, Enugu State, Nigeria
[5] Department of Chemistry and Chemical Technology, School of Science and Technology, Sefako Makgatho Health Sciences University, P. O. Box 94, 0204 Medunsa, Republic of South Africa
[6] Directorate: Postgraduate Studies, Central University of Technology, Free State, Private Bag X 20539, 9300 Bloemfontein, Republic of South Africa
* Corresponding author, e-mail: danladielibako@gmail.com

Received: 02 November 2025, Accepted: 26 January 2026, Published online: 12 February 2026

Abstract

Solid state dye-sensitized solar cells (ssDSSCs) are attracting increasing attention due to their affordable manufacturing, adaptability to lightweight and flexible applications. This present work utilized solar capacitance simulation software to examine the performance of ssDSSCs with both Al^{3+} doped and undoped TiO_2 electron transport layer (ETL). The pure titanium dioxide based device gave an open circuit voltage V_{oc}, short circuit current density J_{sc}, fill factor FF and power conversion efficiency PCE 0.95 V, 15.16 mA cm^{-2}, 64.49% and 9.30%, respectively, while the aluminium doped TiO_2 presents 0.87 V, 18.53 mA cm^{-2}, 68.73% and 11.09% as V_{oc}, J_{sc}, FF and PCE, respectively. This shows that Al^{3+} doped ETL was more promising. The effects of using different hole transport layers (HTLs) were studied. Delafossite (Mg-$CuCrO_2$) was found to be the most potential HTL to dramatically improve device performance with V_{oc} 0.87 V, J_{sc} 19.16 mA cm^{-2}, FF 68.52% and PCE 11.44%. The performance of the fluorine-doped tin oxide (FTO)/Al-TiO_2/N719/Mg-$CuCrO_2$/C device was optimized by varying the ETL thickness and doping concentration, dye thickness and defect density, HTL thickness and doping concentration to obtain 0.16 µm, 10^{20} cm^{-3}, 0.9 µm, 10^{13} cm^{-2}, 0.6 and 10^{22} cm^{-3} as optimal values, respectively. This showed a noticeable performance with optimized PCE 23.75%, supported with FF 84.98%, J_{sc} 24.12 mA cm^{-2} and V_{oc} 1.16 V. The effect of series and shunt resistances, temperature, metal work function, capacitance and Mott-Schottky plot were evaluated and found to affect the optimized device.

Keywords

dye sensitized solar cells, SCAPS-1D, dopant, charge transport layers

1 Introduction

The global society is faced with energy crisis due to the demand and finite nature of nonconventional resources. Presently, the energy demand is made by approximately 85% of fossil fuels which possess a great danger to humanity [1]. Attempt to decarbonize the current energy usage has triggered a vigorous search for novel technology which are available, accessible and clean. Solar energy presents itself as the most available eco-friendly

Cite this article as: Danladi, E., Koao, L. F., Egbuhuzor, M. O., Motaung, T. E., Motloung, S. V. "The Interplay between Dopant and the Surface Structure of an Electron Transport Layer in N719 Solid State Dye-Sensitized Solar Cells: An Analysis of Aluminum-doped Faceted TiO_2 with Mg-$CuCrO_2$ Transport Channels Using the SCAPS-1D Framework", Periodica Polytechnica Chemical Engineering, 70(1), pp. 64–87, 2026. https://doi.org/10.3311/PPch.42701

source in comparison to other sources [2]. Converting solar energy into useful electrical energy requires the use of photovoltaic technologies which have evolved into three generations. The third generation solar cells otherwise called excitonic devices, have gained prominence in the photovoltaic domain due to their simple fabrication process, cost effectiveness, lightweight, lack of requirement for high temperatures and vacuum in films creation and nearly zero requirement for high energy-consuming processes resulting to low payback time [3, 4]. These include:

1. dye sensitized solar cells,
2. quantum dots sensitized solar cells,
3. perovskite solar cells, and
4. organic photovoltaic [5, 6].

Recently, these photovoltaic technologies have been greatly studied, with perovskite solar cell (PSC) being the rising star due to its advantages which include; high absorption coefficient, tunable bandgap, small exciton binding energy, and long diffusion length [3, 7–10]. Its present record efficiency has exceeded 26% which is comparable to the monocrystalline silicon cell [5, 11]. However, its deployment into real world application has been plagued with some limitations which include the presence of poisonous lead and instability of the perovskite layer [12, 13].

The dye sensitized solar cells (DSSCs) have demonstrated effectiveness in ambient conditions [3]. The DSSC is made up of the photoactive layer which consists of the dye molecules adsorbed on the mesoporous semiconductor coated on glass substrate, a counter electrode composed of a catalyst and finally a redox couple that infiltrate the space between the two. For the device to perform comparably better than its silicon-based counterpart, there is need to look into critical issues such as poor power conversion efficiency (PCE) and environmental instability, of which several researches have been expended [4]. Several efforts to include utilization of ruthenium-free organic dyes, the replacement of expensive transparent conductive oxide (TCO) with less expensive ones, replacement of liquid electrolyte with solid state electrolyte and the use of Pt-free catalyst for the counter electrodes [14–16].

The configuration of the solid state dye sensitized solar cell (ssDSSC) has the dye sandwiched between electron transport layer (ETL) and the hole transport layer (HTL). In the configuration, the electrons are conveyed by the ETL and the holes are transported by the HTL [6]. These crucial layers provide outstanding support for the dye molecules, however, to attain to an optimal performance with high stability, there is need to alter the bulk defect properties, carrier concentration and thickness of the device [17]. The presence of large series resistance can prevent electron transport even though at thicker ETL there may be lesser recombination. Titanium dioxide has been established to be the commonly used ETL in solar cells among several metal oxides ETLs [3, 6, 9, 18, 19]. The TiO_2 has a good prospect in charge collection and transfer and also its conduction band edge typically aligns with that of most dye molecules [4, 6, 16]. Also, as a result of its nanocrystalline properties, it undergoes modification through doping or treatment with other foreign materials, making them possess numerous applications in photocatalysis, water splitting etc. [20, 21]. The TiO_2 has high stability, high electron mobility, and transparency in the visible light region of electromagnetic spectrum [17]. These aforementioned properties result to efficient transport of electrons from the harvesting material in solar cells to the metal electrode for high performance device.

On the contrary, its usage has been limited due to a number of challenges which include; its poor conductivity and large defects that uncontrollably results to charge recombination [17, 22]. Improving the performance of TiO_2 ETL requires several initiatives to include; doping, surface treatment, development of nanostructures, and interface engineering [17, 20, 21, 23]. Several materials such as magnesium, samarium, cobalt, lithium, neodymium, and zinc, have been utilized as dopants in TiO_2 to cause a deformation [17, 23–26]. The materials will therefore act as dopants to increase conductivity while preserving exceptional transparency in the visible light region [17, 26].

Due to the direct impact it has as a substrate on the morphology of ssDSSC, the quality of the TiO_2 compact layer is highly indispensable for consideration in developing high performing ssDSSC device. Additionally, as discussed previously, improving the capacity of the ETL to extract electrons efficiently and improve conductivity have great influence on the series resistance reduction and subsequently improving the efficiency [24].

Rafieh et al. [24], first doped TiO_2 with Al^{3+} and Mg^{2+} ions using sol-gel method. This doping process was achieved based on the fact that their ionic radii are comparable to that of Ti^{4+}, and they can replace Ti^{4+} in the lattice position without causing distortion. The presence of the dopants helps to overcome the oxygen vacancies limitations, offsets the bandgap, minimizes the surface and trap states, and reduces the electron-hole recombination rate, which enhances electron transport properties resulting to improved PCE.

With regard to stability concern, the proper choice of HTL should not be overlooked. The HTL is required in

an ssDSSCs to avoid moisture content from having their way into the device to cause degradation. The commonly used organic HTLs are 2,2′,7,7′-tetrakis(N,N-di-*p*-methoxyphenylamine)-9,9′-spirobifluorene (Spiro-OMeTAD), poly[bis(4-phenyl)(2,4,6-trimethylphenyl)amine (PTAA), poly(3-hexylthiophene) (P3HT) and poly[3-(5-carboxypentyl)thiophene-2,5-diyl] (P3CPenT) etc. [10, 15, 27, 28]. These materials are mostly hygroscopic in nature which degrade faster and have lower electrical properties which often require additive treating or doping to improve its conductivity. Also, the difficulties in their synthesis and high material cost have prevented their widespread application for large production [12]. The inorganic HTLs have gain global attention due to their cost effectiveness, stability, and availability [28]. Transitional based HTLs such as chromium oxide (CrO_x), cobalt oxide (CoO_x), molybdenum oxide (MoO_x), vanadium oxide (VO_x), cuprous oxide (Cu_2O), etc. [12, 29, 30] have shown good stability prospect but constrained with PCE of <20% in perovskite solar cells. In addition, HTLs such as, copper(I) thiocyanate (CuSCN), copper antimony sulfide ($CuSbS_2$), copper iodide (CuI), copper(II) sulfide (CuS), and copper(I) selenocyanate (CuSeCN), etc. are viable HTLs for high efficiency solar cells [6, 31], however, they are characterized with poor electrical properties such as low hole mobility, low conductivity, difficult method of application, and low stability. The ternary metal oxides represented as ABO_2, in which "A" represents a monovalent positive ion and "B" represents a trivalent positive ion have gained attention. Some of the examples include; palladium cobalt oxide ($PdCoO_2$), copper cobalt oxide ($CuCoO_2$), copper chromium oxide ($CuCrO_2$), silver aluminum oxide ($AgAlO_2$), platinum cobalt oxide ($PtCoO_2$), copper gallium oxide ($CuGaO_2$) and copper scandium oxide ($CuScO_2$), which are categorized as a subgroup of delafossite minerals [12]. However, among all the *p*-type delafossites, copper chromium oxide is exceptional due to its good transparency ~90% [32, 33], good hole mobility 33.91 $cm^2\ V^{-2}\ s^{-1}$ [33, 34], a range of bandgap 3.1–3.35 eV and conductivity ranging from 10–230 Scm^{-1} [35, 36]. The copper-based delafossites are considered as viable HTLs for solar cell due to their superior thermal and chemical stability, deep valence band edge, and suitable band energy matching [35]. However, reports on these materials have seldom been documented in literatures.

Hence, in this study, the performance of both Al^{3+} doped and undoped TiO_2 ETLs are investigated in ssDSSCs to obtain optimal configuration in fluorine-doped tin oxide (FTO)/ETL/N719/HTL/C architecture. This helps to evaluate the potential improvements brought about by the treatment of TiO_2 compared with its untreated counterparts through numerical simulation using solar capacitance simulator in one dimension (SCAPS-1D [37]). The effects of using different HTLs was studied. We subsequently investigated the effect of ETL thickness and doping concentration, dye thickness and defect density, HTL thickness and doping concentration, shunt and series resistance, temperature and Mott-Schottky analysis. The study shows that Al^{3+} doped ETL was more promising. Also, delafossite (Mg-$CuCrO_2$) HTL is a potential material to dramatically improve device performance. The study proposed two competitive and attractive configurations for ssDSSCs high-efficiency devices, opening up useful research opportunities for designing and manufacturing high-efficiency and reasonably cost-effective solar cells. Among those structures, the Al-TiO_2 ETL showed noticeable performances with optimized PCE 23.75%, supported with fill factor FF 84.98%, short circuit current density J_{sc} 24.12 mA cm^{-2} and open circuit voltage V_{oc} 1.16 V. This shows that the treatment TiO_2 with Al^{3+} resulted in a band offset, leading to enhanced band alignment. This band alignment is crucial as it minimizes recombination defects, thereby improve the flow of charge carriers and ultimately enhance device performance.

2 Materials and methods

The field of photovoltaics has recorded unprecedented progress due to several numerical tools that simplified the developmental process [38]. One of the most used is the solar capacitance simulator developed by a group of researchers at the Ghent University, Belgium [39]. In science and engineering, modeling and simulation is a critical aspect in realizing efficient and economical viable photovoltaic technology. A number of benefits are attached to it which include, time saving, accurate prediction and optimization [16, 40]. The SCAPS-1D [37] simulator can simulate the properties of the solar cell electrically which include; the current-voltage properties, capacitance-voltage properties, quantum efficiency and capacitance-frequency characteristic [41] which are vital for device optimization. By modeling a solar cell comprehensively, optimal configuration of solar device can be obtained, which can give the live-line for high performing device. Over the years, several modifications within the SCAPS-1D [37] user interface have been made to capture defect modeling, interfacial recombination, grading, tunneling, temperature alteration which has given rise to high accuracy during simulation and paved the way for

broader application. Since the advent of SCAPS-1D [37], it has created deep theoretical insight for understanding the mechanism of photovoltaics and also assisted experimentalists in designing and fabricating solar cells [8, 39]. The tool basically works by solving the basic semiconductor equations iteratively while tackling the concentration of both holes and electrons linearly [19]. For the simulation to replicate its real counterpart, the input parameter must be chosen with precision. The Poisson equation is shown in Eq. (1), while the continuity equations are shown in Eqs. (2) and (3) [8, 10]:

$$\frac{d^2}{dx^2}\psi(x) = \frac{q}{\varepsilon_0 \varepsilon_r}\left[p(x) - n(x) + N_D - N_A + \rho_P - \rho_n\right] \quad (1)$$

$$\frac{\partial n}{\partial t} = \frac{1}{q}\frac{\partial J_n}{\partial x} + \left(G_n - R_n\right) \quad (2)$$

$$\frac{\partial p}{\partial t} = \frac{1}{q}\frac{\partial J_p}{\partial x} + \left(G_p - R_p\right) \quad (3)$$

where ψ = electrostatic field, $n(x)$ = carrier density of electron, $p(x)$ = carrier density of hole, ε_r = relative permittivity, ε_0 = free-space permittivity, N_D = donor impurity concentration, N_A = acceptor, the hole and electron distributions are represented by ρ_P and ρ_n respectively, q = electric charge, G = rate of generation, R = rate of recombination, J_n = electron density and J_p = hole density.

Equations (4) and (5) can be used to measure the fill factor and the efficiency of the device:

$$\mathrm{FF} = \frac{J_{mp}V_{mp}}{J_{sc}V_{oc}} \quad (4)$$

$$n = \frac{J_{sc}V_{oc}\mathrm{FF}}{P_{in}} \quad (5)$$

where J_{mp} = maximum obtainable current, V_{mp} = maximum obtainable voltage, J_{sc} = short circuit current, V_{oc} = open circuit voltage.

It is crucial to note that the recombination rates for electrons and holes encompass both radiative processes and recombination through deep-level traps. The Shockley–Read–Hall (SRH) formalism is used to evaluate recombination mechanism. The SRH recombination rate R_{SRH}, which is expressed in Eq. (6), depends on the lifetime of the minority carrier (τ). The SRH method also takes into account the effect of defect states through the defect density, as shown in Eq. (7):

$$R_{\mathrm{SRH}} = \frac{\left(np - n_i^2\right)}{\tau\left(p + n + 2n_i \cosh\left(\frac{E_i - E_t}{k_B T}\right)\right)} \quad (6)$$

$$\tau = \frac{1}{\sigma N_t v_{th}}. \quad (7)$$

E_t is the position of the trap energy level and the intrinsic level is represented by E_i. T is the absolute temperature. The k_B is the Boltzmann constant. The σ is the capture cross-section for electrons or holes, N_t is the defect density and the v_{th} is the thermal speed.

The following standard conditions were utilized in carrying out the simulation; light illumination of 100 mW cm^{-2}, frequency of 1×10^{16} Hz, temperature of 298.15 K. The interface defect layer was introduced in the ETL/N719 interface for interfacial recombination on the

Table 1 Data for individual layer used for the simulation of the ssDSSc [16, 23, 41–43]

Parameters	FTO	TiO_2	Al-TiO_2	N719	CuSCN
Thickness (μm)	0.3	0.05	0.05	0.6	0.3
Band gap energy E_g (eV)	3.5	3.2	3.0	2.33	3.4
Electron affinity χ (eV)	4.0	4.2	3.62	3.9	1.7
Relative permittivity ϵ_r	9.0	10.0	19.6	30	10.0
Effective conduction band density N_c (cm^{-3})	2.2×10^{18}	2.2×10^{18}	2.2×10^{18}	2.4×10^{20}	2.2×10^{19}
Effective valance band density N_v (cm^{-3})	1.8×10^{18}	1.8×10^{19}	1.8×10^{18}	2.5×10^{20}	1.8×10^{18}
Electron thermal velocity (cms^{-1})	20	20	20	5	100
Hole thermal velocity (cms^{-1})	10	10	10	5	25
Electron mobility μ_n (cm^2 V^{-1} s^{-1})	1×10^7	1×10^7	1×10^7	1×10^7	1×10^7
Hole mobility μ_p (cm^2 V^{-1} s^{-1})	1×10^7	1×10^7	1×10^7	1×10^7	1×10^7
Donor concentration N_D (cm^{-3})	2×10^{19}	1×10^{17}	1×10^{18}	0	0
Acceptor concentration N_A (cm^{-3})	0	0	0	1×10^{17}	1×10^{18}
Defect density N_t (cm^{-3})	1×10^{15}	1×10^{15}	1×10^{14}	1×10^{15}	1×10^{15}

photovoltaic performance. Table 1 shows the data for different layers which were obtained from previously documented [16, 23, 41–43]. Table 2 [16, 44] and Table 3 [10, 16, 41, 42] show the data for defect interface and various HTLs. The interface data were obtained from the work of Danladi et al. [44] and Tariq et al. [16] which involved both density functional theory and SCAPS-1D [37] study. At the surface and at every interface, the optical reflectance is regarded as zero [45]. The schematic representation of the modeled device is shown in Fig. 1.

3 Results and discussion

3.1 Effect of substituting TiO_2 with Al-TiO_2

To explore the impact of replacing TiO_2 with Al-TiO_2, we simulated the device in the dark and light conditions. Fig. 2 (a) shows the current-voltage (*J-V*) curve under illumination, Fig. 2 (b) shows the *J-V* curve in the dark, while Fig. 2 (c), (d) shows the energy band diagram of Al doped TiO_2 and pure TiO_2. In this study, the effective photons coupling to the ruthenium dye (N719) are same for Al doped TiO_2 and pure TiO_2. To validate and test the effectiveness of our simulation, a calibration was carried out based on the work of Premalal et al. [46] and compared. Table 4 shows the comparison between experimental and simulations data in terms of V_{oc}, J_{sc}, FF and PCE. The pure TiO_2 based device gave a V_{oc}, J_{sc}, FF and PCE of 0.95 V, 15.16 mA cm^{-2}, 64.49% and 9.30%, while the Al doped TiO_2 presents 0.87 V, 18.53 mA cm^{-2}, 68.73% and 11.09% as V_{oc}, J_{sc}, FF and PCE. Other devices in the Table 4 shows a PCE of 4.24% [46], 2.10% [47], 5.38 [43], and 5.71% [41] (see Fig. 3). The Al modified device is observed to have enhanced performance over device without Al. When Al^{3+} replaced Ti^{4+} in the TiO_2 lattice, it generated oxygen vacancies or free carriers (electrons) to keep the charge neutral. This leads to a larger carrier concentration and better conductivity of TiO_2, which lowers series resistance and enhances electron transport [17]. The Al doping passivated surface trap states and defects in TiO_2, which made it less likely for electrons and holes to recombine at the TiO_2/N719 interface. TiO_2 isn't the major material that absorbs light, but adding Al can make the film better by reducing scattering losses and making the grain boundaries smaller and the morphology smoother. This allows sufficient light to get to the absorber dye, which raises J_{sc}.

Table 2 Data used for the interface layer [16, 44]

Parameters	Absorber	ETL/N719	HTL/N719
Defect type	Neutral	Neutral	Neutral
Capture cross section for electron (cm^2)	1×10^{-15}	1×10^{-19}	1×10^{-19}
Capture cross section for hole (cm^2)	1×10^{-15}	1×10^{-19}	1×10^{-19}
Energetic distribution	Gaussian	Single	Single
Energy level with respect to E_v (eV)	0.600	0.600	0.600
Characteristic energy (eV)	0.1	0.1	0.1
Total density (cm^{-3})	1×10^{14}	1×10^{10}	1×10^{10}

Table 3 Data for individual layer used for the simulation of the solar cell [10, 16, 41, 42]

Parameters	CuSCN	CuO	Cu_2O	$CuSbS_2$	$CuCrO_2$	$MgCuCrO_2$
Thickness (μm)	0.3	0.3	0.3	0.3	0.3	0.3
Band gap energy E_g (eV)	3.4	1.5	2.2	1.58	3.29	3.06
Electron affinity χ (eV)	1.7	4.07	3.4	4.2	2.2	2.2
Relative permittivity ϵ_r	10.0	18.1	7.5	14.6	10.8	3.0
Effective conduction band density N_c (cm^{-3})	2.2×10^{19}	2.2×10^{19}	2.0×10^{19}	2.0×10^{18}	2.2×10^{18}	2.5×10^{18}
Effective valance band density N_v (cm^{-3})	1.8×10^{18}	5.5×10^{20}	1.0×10^{19}	1.0×10^{19}	8.0×10^{20}	1.8×10^{19}
Electron thermal velocity (cms^{-1})	100	100	200	49	2.0×10^{-2}	8.0×10^{-2}
Hole thermal velocity (cms^{-1})	25	0.1	8600	49	2.0×10^{-2}	8.0×10^{-2}
Electron mobility μ_n (cm^2 V^{-1} s^{-1})	1×10^{7}	1×10^{7}	1×10^{7}	1×10^{7}	1×10^{7}	1×10^{7}
Hole mobility μ_p (cm^2 V^{-1} s^{-1})	1×10^{7}	1×10^{7}	1×10^{7}	1×10^{7}	1×10^{7}	1×10^{7}
Donor concentration N_D (cm^{-3})	0	0	0	0	0	0
Acceptor concentration N_A (cm^{-3})	1×10^{18}	1×10^{18}	1×10^{18}	1×10^{18}	1×10^{19}	1×10^{19}
Defect density N_t (cm^{-3})	1×10^{15}	1×10^{15}	1×10^{15}	1×10^{15}	1×10^{15}	1×10^{15}

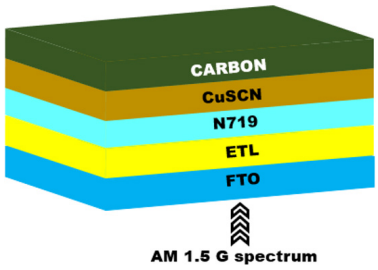

Fig. 1 Solar cell configuration, where AM 1.5 is the solar intensity

The energy bandgap in Fig. 2 (c), (d) were utilized to explore the effect of changing TiO_2 with Al-TiO_2 as electron transport layer. In comparison, the Al doping marginally pushes the conduction band edge of TiO_2 downward, whereas the offset was nonexistent in the pure TiO_2 ETL. The energy band reveals that the resistance at the Al-TiO_2/N719 interface is smaller than that at the TiO_2/N719. This enhances energy-level matching with the dye

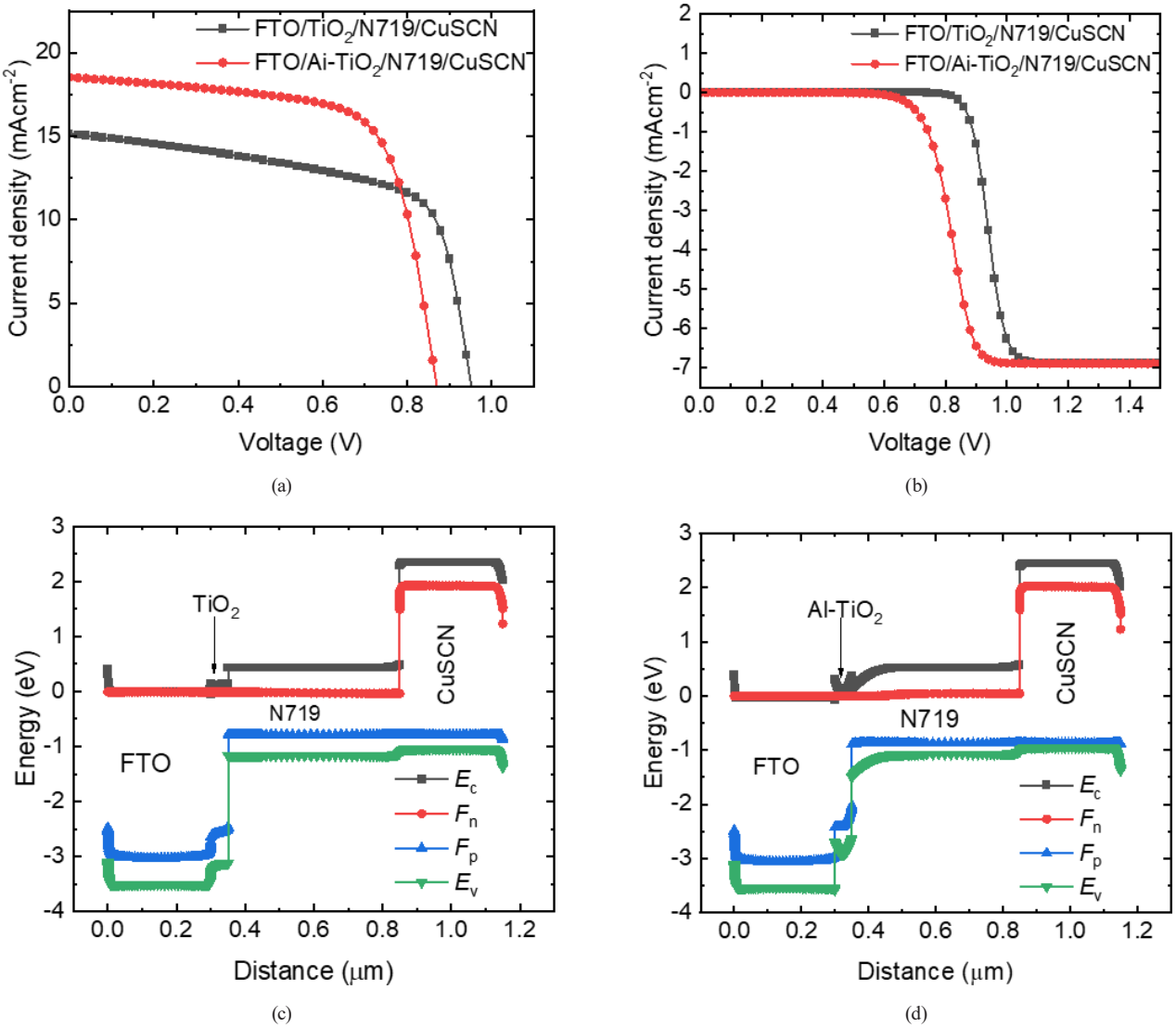

Fig. 2 (a) *J-V* curve for TiO_2-based and Al-TiO_2-based device under illumination, (b) *J-V* curve for TiO_2-based and Al-TiO_2-based device under dark condition, (c) Energy band profile for TiO_2-based device, (d) Energy band profile for Al-TiO_2-based device

Table 4 *J-V* parameters of experimental and simulated outcomes

Device	Configuration	Study	V_{oc} (V)	J_{sc} (mA cm^{-2})	FF (%)	PCE (%)	Remark
A	FTO/TiO_2/N719/CuSCN/C	Exp.	0.65	15.76	41.60	4.24	[46]
B	FTO/P-TiO_2/N719/CuSCN/G	Exp.	0.60	7.80	44.00	2.10	[47]
C	FTO/PCBM/N719/CuCSN/Au	Sim.	0.89	8.56	70.94	5.38	[43]
D	FTO/TiO_2/N719/CuSCN/Pt	Sim.	1.17	6.23	78.32	5.71	[41]
E	FTO/TiO_2/N719/CuSCN/C	Sim.	0.95	15.16	64.49	9.30	[This work]
F	FTO/Al-TiO_2/N719/CuSCN/C	Sim.	0.87	18.53	68.73	11.09	[This work]

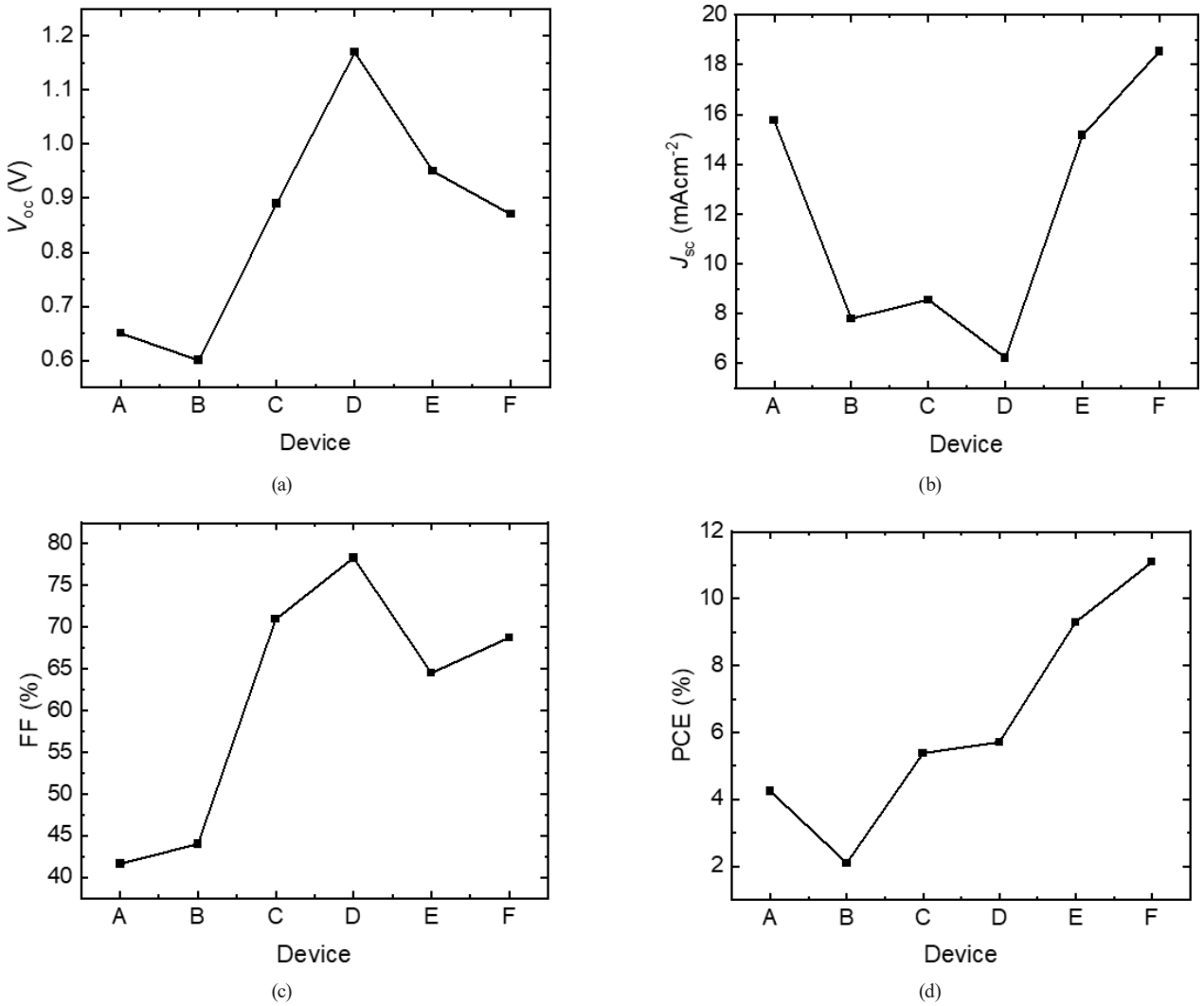

Fig. 3 Relationship showing (a) V_{oc}, (b) J_{sc}, (c) FF, and (d) PCE with experimental or simulated device

and promotes effective electron injection from the dye to TiO_2. The presence of Al dopant has no effect on its oxidation state in the TiO_2 material. There was discrepancies between the valence band edge of the two ETLs. A higher band inset is found on the valence band maximum edge of the Al doped TiO_2 ETL. This changes in the conduction band maximum have impact on the photovoltaic output of the device. The aluminum doped device gave a proper band matching, which permits extracted electron to be blocked by the HTL and the extracted hole to be blocked by the ETL. This allows the charge transfer go to the appropriate channels with little interface recombination. The Al-TiO_2 modified device was considered for further optimization on the ssDSSCs.

3.2 Optimization of hole transport layer of the N719 solid state dye-sensitized solar cell

The hole transport layer is one of the most critical components of ssDSSC. It inhibits electrons from flowing through and transfers holes to the metal electrode [48]. To have an efficient HTL in a ssDSSC device, the band gap, thickness, and doping concentration of the HTL must be chosen carefully and correctly [16, 49]. The data in Table 3 was utilized for the HTL optimization. The results are presented in Fig. 4 (a), (b). Fig. 4 (a) illustrates the current voltage curve for the device with various inorganic HTLs, while Fig. 4 (b) shows the power density (*P*) against the voltage for all the HTLs. The energy band profiles are provided in Fig. 4 (c).

A total of 6 HTLs were used which include; CuSCN, CuO, Cu_2O, $CuSbS_2$, $CuCrO_2$ and Mg-$CuCrO_2$. The devices delivered PCEs between 5.87 and 11.44%. The ssDSSCs with CuSCN, CuO, $CuCrO_2$ and Mg-$CuCrO_2$ demonstrate higher PCE over the devices with Cu_2O and $CuSbS_2$ HTLs which is attributed to the wider band gaps and better-aligned valence band positions, enabling efficient hole extraction and effective electron blocking, high valence band offset, divergence in energy alignment between the

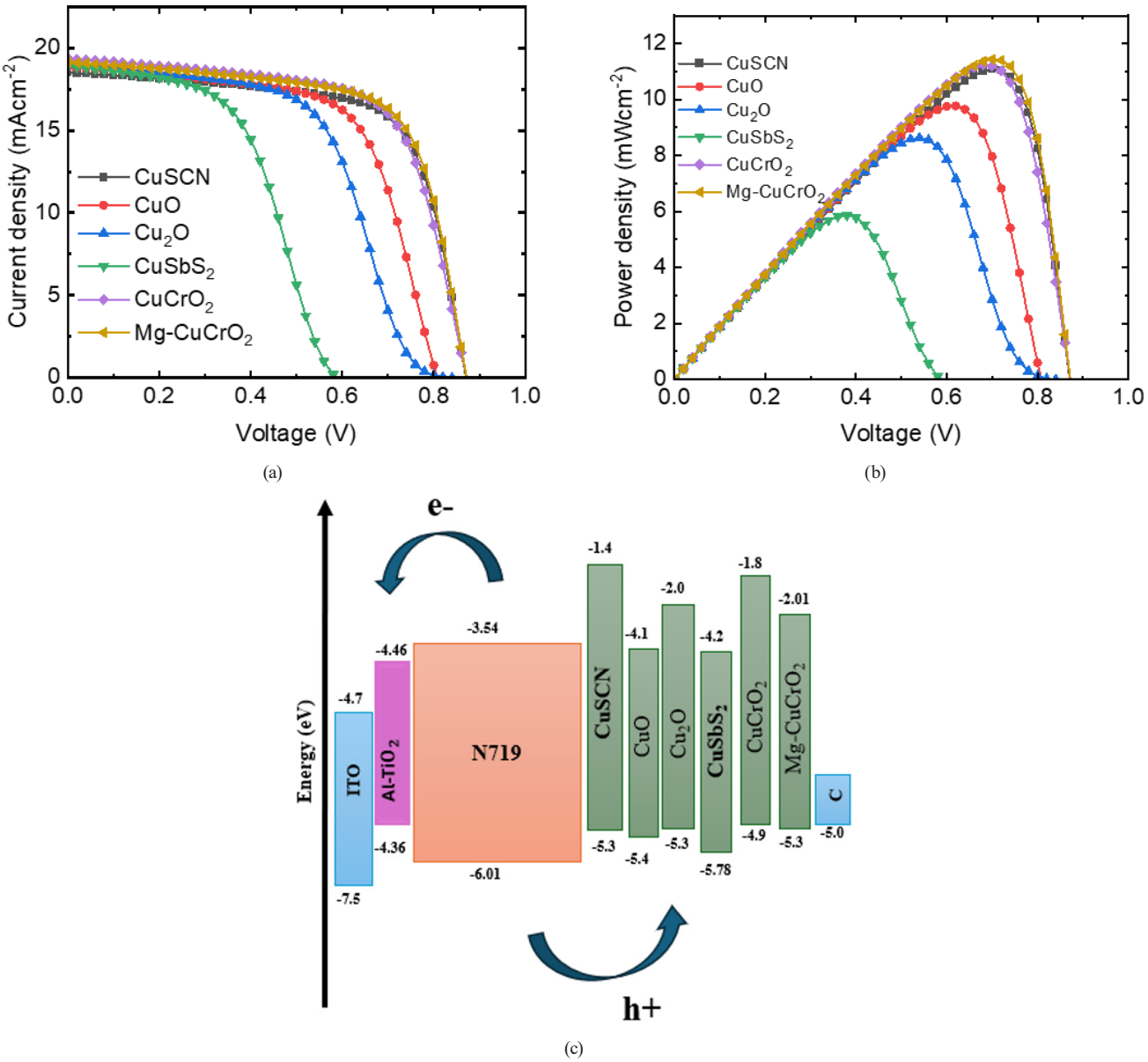

Fig. 4 *J-V* curve with various HTLs under illumination (a); *P-V* curve with various HTLs under light condition (b) and Energy band alignment for different HTLs (c) (ITO: indium tin oxide)

valence band (VB) of the HTLs with that of the absorber, which enable energy level mismatch that facilitate recombination processes [12, 50]. The Cu_2O and $CuSbS_2$ often create unfavorable offsets and more recombination leading to inferior performance. CuSCN and $CuCrO_2$/Mg–$CuCrO_2$ are transparent in the visible, so they don't deprive photons, couple with their good conductivity that lowers resistance, unlike the Cu_2O and $CuSbS_2$ that tend to be rich in defect, with poor transport and higher recombination. The best performing device was with Mg-$CuCrO_2$ hole conductor giving a V_{oc} of 0.87 V, J_{sc} of 19.16 mA cm^{-2}, FF of 68.52%, and PCE of 11.44%. This might be ascribed to the higher hole conductivity, lower surface roughness, resulting to enhanced light absorption and contact, alongside the well-matched energy level alignment with the N719 dye. All of these lessens the charge transport pathways and minimizes recombination thereby improving light harvesting, charge transport and overall PCE. Summarily, for the structure FTO/Al-TiO_2/N719/HTL/C, the order of efficiency is as follows: Mg-$CuCrO_2$ (11.44%) > $CuCrO_2$ (11.24%) > CuSCN (11.09%) > CuO (9.77%) > Cu_2O (8.63%) > $CuSbS_2$ (5.87%).

When two materials come into contact, their energy levels align, influencing the movement of electrons and holes across the interface. This is demonstrated by the band alignment. For many applications, including solar

cells and transistors, this is essential [16, 51]. The two primary forms of band alignment are Type I (cliff) and Type II (spike) [17]. Each type has a different effect on charge flow across the interface. Effective electron movement from a higher to a lower energy level is made possible, for instance, in a Type I alignment, where the VB maximum of one material is lower than or aligned with the conduction band (CB) minimum of the other material [16].

The electron (F_n) and hole (F_p) quasi-fermi levels are the two levels that are produced when light strikes the device. This merely confirms that electron-hole (*e-h*) pairs have been created inside the solar device. According to Fig. 5, F_n is represented by the location between the conduction band (E_c) and the electron energy level, and F_p is represented by the location between the valence band (E_v) and the hole energy level. The resistance at the interface, electric fields, and built-in potential at the N719/ETL, N719/HTL are all impacted by the slight offsets in the conduction and valence bands.

The energy band that corresponds to the device is displayed in Fig. 5 (a)–(f), with various HTLs showing the locations of E_v, E_c, F_n, and F_p. The distance in μm is represented by the abscissa, and the energy levels in eV are represented by the ordinate. The band matching across the device's interface, which is defined by either the valence band offset (VBO) associated with the N719/HTL or the conduction band offset associated with the ETL/N719 interface, is the primary factor influencing the metric performance of solar cell. According to Srivastava et al. [52], high efficiencies are typically. Our band simulation results show that the most effective device based on Mg-$CuCrO_2$ HTL has a spike-like transformation, whereas the least effective device based on $CuSbS_2$ HTL has a cliff-like transformation. As a result, in our simulation, the quasi-fermi energy level positions depend on carrier concentrations and nonequilibrium conditions (e.g., illumination or carrier injection).

3.3 Effect of changing electron transport layer thickness and doping concentration on the performance of the perovskite solar cell

The ETL is positioned between the absorbing dye and the FTO, which has a significant effect on the solar cell. Since the dye photon coupling depends on the ETL parameters, it is crucial to examine them. The impact of the ETL's thickness and doping density on the ssDSSC device's performance was examined. To obtain a high-performing solar cell device, it is always essential to obtain the ideal PV metric. To investigate their impact on the device's performance, the donor density was varied from 10^{14} to 10^{21} cm^{-3} and the ETL thickness was varied from 0.02 to 0.16 μm during the device simulation.

The impact of the simultaneous change in N_D and ETL thickness on the V_{oc} of the Al-TiO_2-modified ssDSSC is shown in Fig. 6 (a). There is a slight variation in the contour mapping between 0.8714 and 1.1853 V. In this dataset, the V_{oc} rises with thickness and falls with increasing N_D (i.e., higher N_D results to lower V_{oc}). V_{oc} is dependent on recombination and splitting at the quasi-Fermi level. V_{oc} is increased by a thicker ETL because it can better block holes and lessen interface recombination. However, increasing N_D causes the electron quasi-Fermi level to shift and the depletion width/band bending to decrease, which frequently lowers the built-in potential. It can also increase recombination through increased carrier density, which results in lower V_{oc} at higher N_D. ETL thickness of 0.02 μm and ETL N_D of 10^{18} cm^{-3} had the lowest open circuit voltage value, whereas ETL thickness of 0.16 μm and ETL N_D of 10^{14} cm^{-3} had the highest V_{oc}.

Fig. 6 (b) illustrates how variations in ETL thickness and N_D affect J_{sc}. The J_{sc} has the largest absolute dynamic range of all four metric parameters (0.659 to ~19.245 mA cm^{-2}). Although it tends to fall with greater thickness, the J_{sc} has a positive correlation with ETL N_D. Higher N_D significantly improves the J_{sc} (due to improved electron collection and ETL conductivity). A higher J_{sc} results from a decrease in series resistance and collection losses caused by an increase in ETL N_D's conductivity and electron extraction. The ETL thickness of 0.16 μm and ETL N_D of 10^{14} cm^{-3} produced the lowest J_{sc} value, while the ETL thickness of 0.16 μm and ETL N_D of 10^{20} cm^{-3} produced the highest J_{sc}.

The change in FF as ETL thickness and N_D increase is depicted in Fig. 6 (c). As can be seen, the FF reflects the PCE, with its maximum value of approximately 78.75% at N_D value in the range of 10^{14} cm^{-3} at 0.16 μm thickness. At ETL N_D of 10^{16} cm^{-3} and thickness of 0.01 μm, the lowest FF of approximately 6.49% was obtained. Because the FF is extremely sensitive to resistive losses, doping the ETL helps to extract carriers and moderately reduces the ETL's series resistance, which raises the FF value. Because it increases recombination at the contact/interface, increasing thickness at low ETL N_D decreases FF. However, at low thickness and higher doping density, there was higher charge extraction, which minimizes transport losses and improves FF.

The contour plot of the PCE variation in relation to the changes in ETL thickness and ETL N_D is displayed

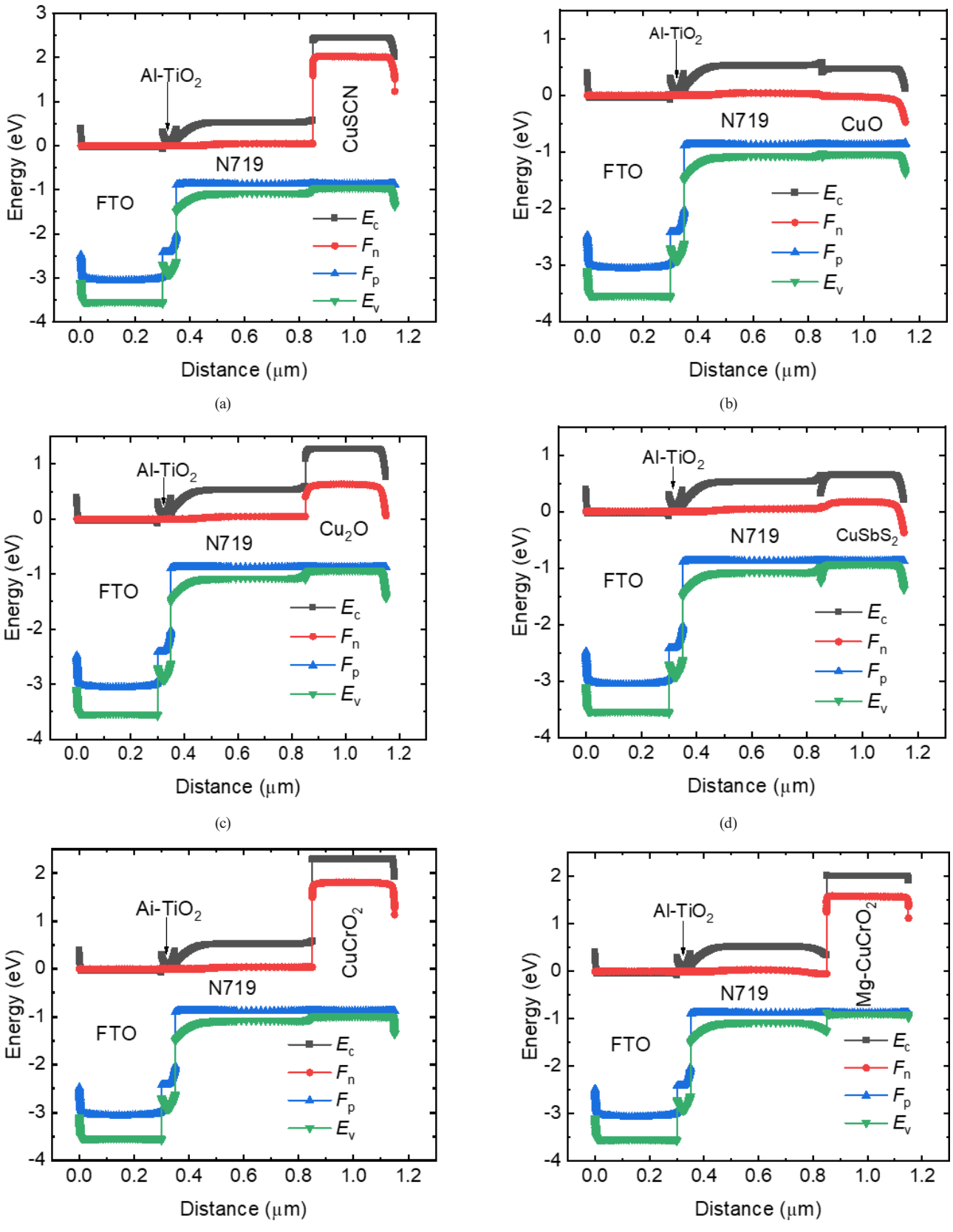

Fig. 5 Energy band diagram of (a) CuSCN, (b) CuO, (c) Cu_2O, (d) $CuSbS_2$, (e) $CuCrO_2$ and (f) Mg-$CuCrO_2$

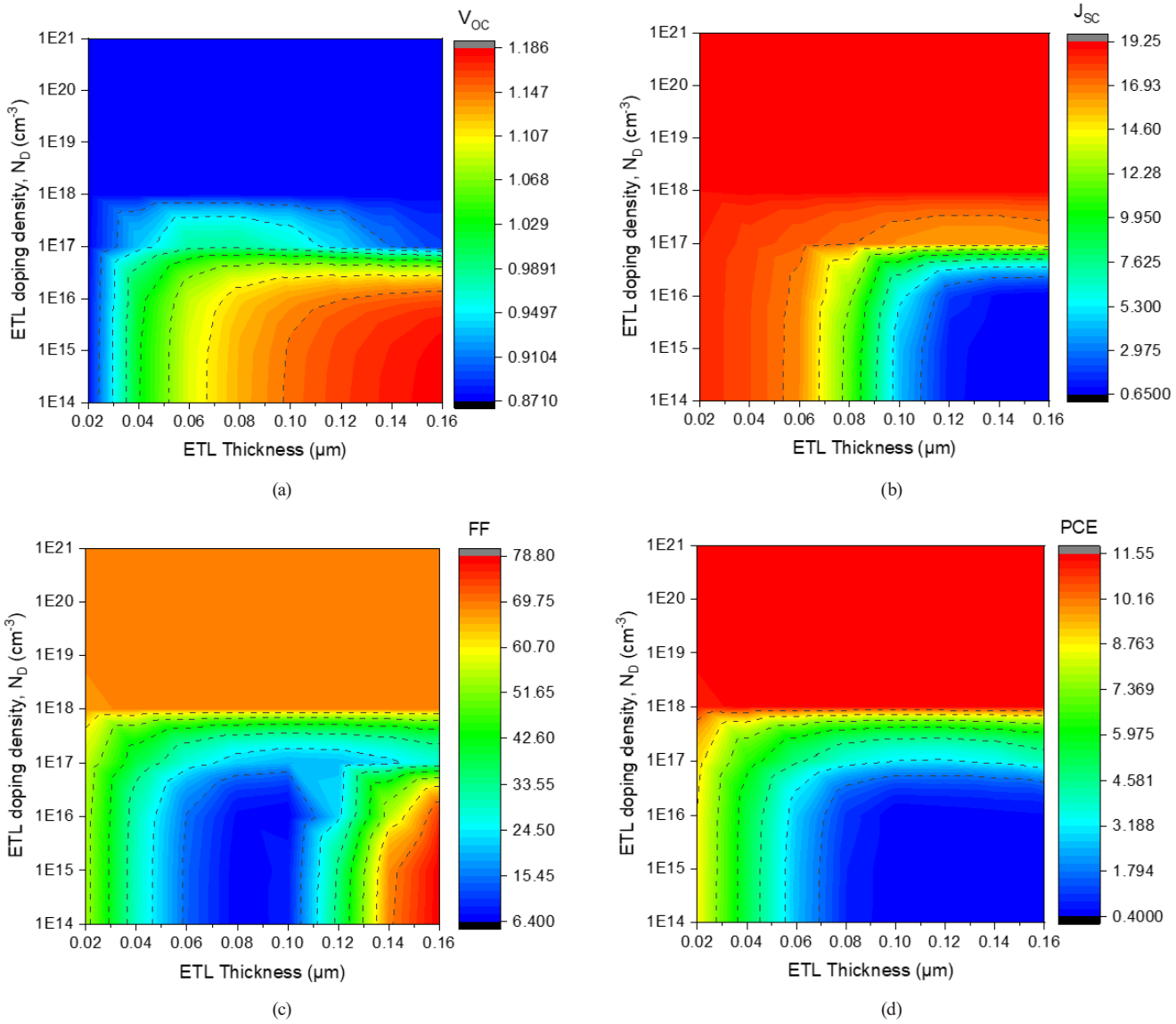

Fig. 6 Contour mapping of ssDSSC device showing (a) V_{oc}, (b) J_{sc}, (c) FF, and (d) PCE on the ETL thickness and ETL doping density

in Fig. 6 (d). As can be seen, when the ETL thickness increased from 0.02 to 0.16 μm, the PCE varied from 0.425% (very poor point) to maximum ~11.542%. Both the ETL N_D and thickness were the main controlling factors on the performance. The device's performance depends on a number of different factors. At thickness = 0.16 μm and doping = 1×10^{20} cm^{-3}, the best PCE was obtained; at ETL $N_D \geq 10^{21}$ cm^{-3}, performance declines. ETL thickness of 0.16 μm and ETL N_D of 10^{20} cm^{-3} are the optimized parameters for best performance, resulting in PCE of 11.542%.

3.4 Effect of changing dye thickness and defect density on the performance of the N719 dye sensitized solar cell

The dye thickness is one of the key elements that affects the solar cell's response. The production of charge carriers can be improved and increased by increasing the dye thickness [16]. In order to determine the ideal value, optimization is typically done to examine the impact of different thicknesses. This implies that careful selection is required. Likewise, the absorbing dye's N_t affects the efficiency of recombination and extraction, necessitating careful selection. Defects like the N719 dye's carboxylic acid groups deprotonating cause anionic carboxylate groups, which change the dye's binding to the TiO_2 surface and its electronic structure, adsorption geometry, and interaction with solvent molecules that are co-adsorbed [53–55]. Through its impact on the electronic coupling between the dye and the semiconductor, this transition to a di-anionic state can alter the dye's light absorption, charge injection efficiency, and the overall performance of the dye-sensitized solar cell [54].

The contour mappings of the solar device are displayed in Fig. 7 in relation to the concurrent changes in dye thickness and defect density in the ranges of 0.4–0.9 μm and

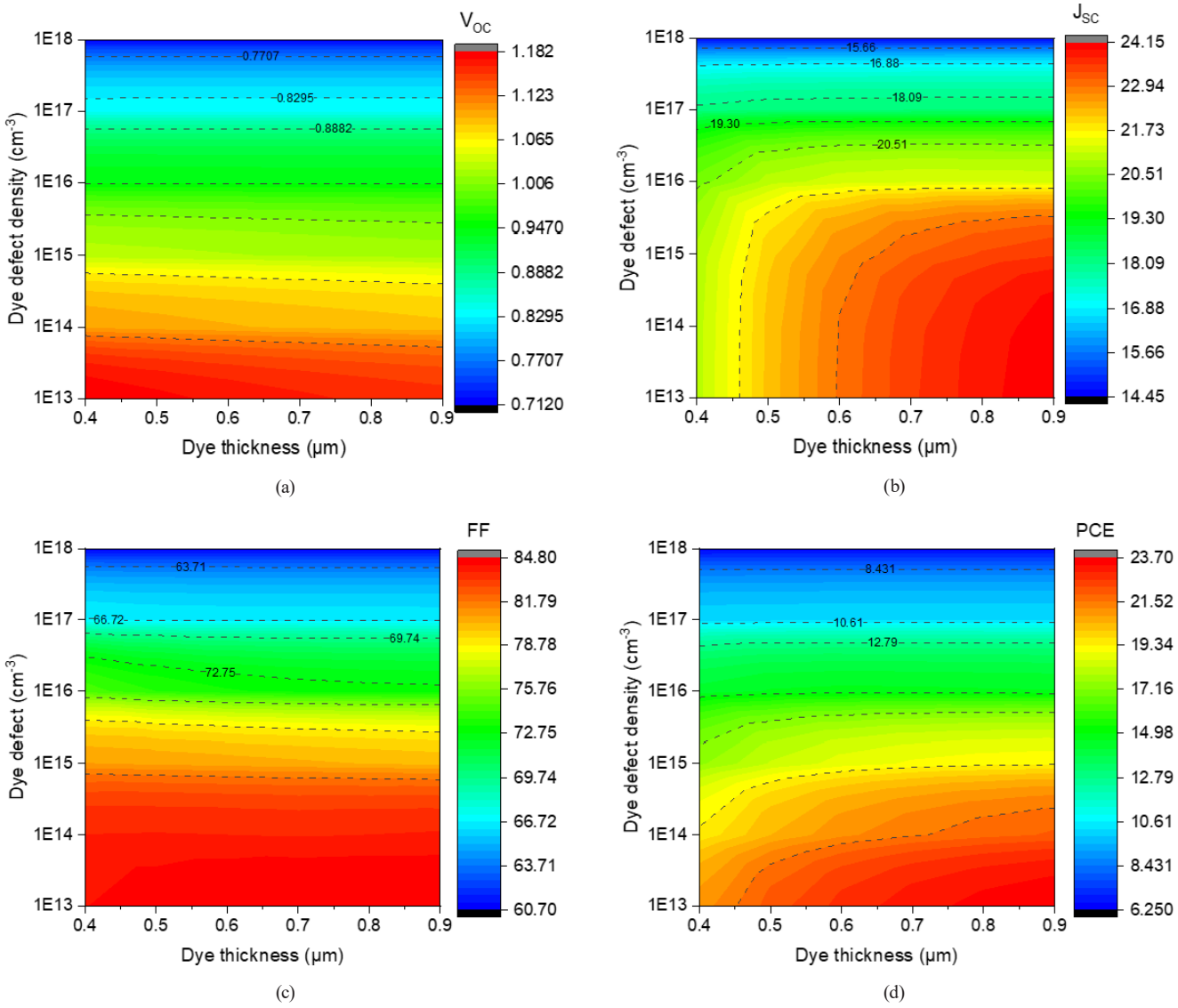

Fig. 7 Contour mapping of ssDSSC device showing (a) V_{oc}, (b) J_{sc}, (c) FF, and (d) PCE on the dye thickness and dye defect density

10^{13}–10^{18} cm^{-2}. For instance, six distinct values of PCE, FF, J_{sc}, and V_{oc} will be recorded if a thickness of 0.2 µm is selected and simulated using 10^{13}, 10^{14}, 10^{15}, 10^{16}, 10^{17}, and 10^{18} cm^{-2}. The contour mapping of the photovoltaic metrics (V_{oc}, J_{sc}, FF, and PCE) in relation to varying the dye thickness and defect concentration is displayed in Fig. 7 (a)–(d). The metric performance was assessed as the thickness was varied between 0.4 and 0.9 µm and the doping concentration was varied between 10^{13} and 10^{18} cm^{-2}. For each of the four-performance metrics (V_{oc}, J_{sc}, FF, and PCE), it produced 47 iterative performance data points, leading to a more precise optimization.

As shown in Fig. 7 (a), as the thickness decreased from 0.9 to 0.4 µm and N_t increased from 10^{13}–10^{19} cm^{-2}, the V_{oc} decreased from 1.182 to 0.573 V. Low defect density (1×10^{13}) results in the highest V_{oc} (~1.182 V), while the thickest film (0.9 µm) and highest defect (1×10^{18}) result in the lowest V_{oc} (~0.573 V). V_{oc} generally exhibits a weakly negative relationship with both defect density and thickness. V_{oc} is especially vulnerable to the quasi-Fermi level splitting and recombination. V_{oc} falls as defect density increases, which is in line with the traditional prediction that higher defect/trap density causes more nonradiative recombination, which lowers V_{oc}.

The change in J_{sc} as absorber thickness and doping density increase is depicted in Fig. 7 (b). As one approaches the high-defect and moderate thickness, the J_{sc} decreases. At thickness = 0.9 µm and defect = 1×10^{13}, the maximum J_{sc} (~24.14 mA cm^{-2}) is reached. At very high defect density and intermediate thickness (defect = 1×10^{18}, thickness = 0.4 µm), the minimum J_{sc} (~14.50) is obtained. Better light harvesting (thicker dye) and better injection/collection (higher effective doping/conductivity) are advantageous for the J_{sc}.

The change in FF as dye thickness and defect density increase is depicted in Fig. 7 (c). The best FF is located close to the high-defect region (peak ≈ 84.73 at defect = 1 × 10^{18}, and thickness = 0.8 µm), which is in line with the J_{sc} trend. Reducing recombination at the interface and series resistance/transport losses both improve the FF. The low "defect" values in this work seem to be related to better conductivity or charge extraction.

The variation in PCE as an augmenting function of absorber thickness and doping density is displayed in Fig. 7 (d). Low nominal defect densities (e.g., 1 × 10^{13}) at moderately large thicknesses (~0.8–0.9) yield the highest efficiencies. The high-defect, low thickness (defect = 1 × 10^{18}, thickness = 0.4 µm) exhibits the lowest efficiencies. Efficiency generally has a weak negative correlation with thickness, indicating a strong interaction with defect density. At thickness = 0.9 µm and defect = 1 × 10^{13}, the maximum PCE was 23.67%.

3.5 Effect of hole transport layer thickness and hole transport layer acceptor concentration

The impact of the HTL thickness and its N_A on the solar device's output was examined. To get a high-performing ssDSSC device, it is always essential to obtain the ideal PV metric. To investigate their impact on the device's performance, the acceptor density was varied from 10^{17} to 10^{22} cm^{-3} and the HTL thickness was varied from 0.1 to 0.6 µm during the device simulation. The contour mapping of the N719 ssDSSC's performance metrics (V_{oc}, J_{sc}, FF, and PCE) is displayed in Fig. 8 (a)–(d). This demonstrates how the modeled device's HTL thickness and N_A have an impact simultaneously. Fig. 8 (a) shows that

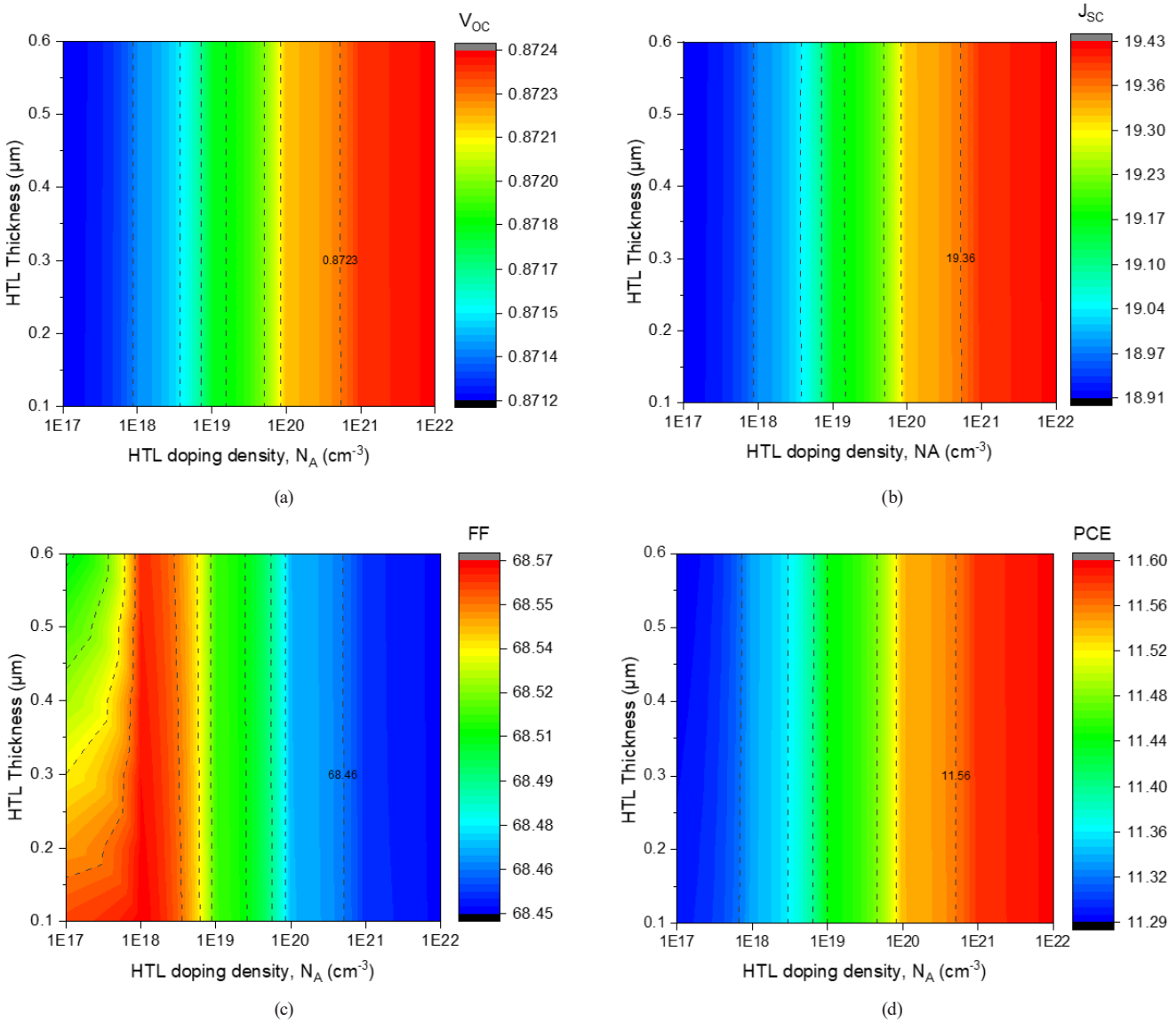

(a) (b) (c) (d)

Fig. 8 Contour mapping of PSC device showing (a) V_{oc}, (b) J_{sc}, (c) FF, and (d) PCE on the HTL thickness and HTL doping density

when the thickness increased from 0.1 and 0.6 μm with N_A increasing from 10^{17} to 10^{22} cm^{-3}, the V_{oc} increased from 0.8704 to 0.8770 V. Additionally, the V_{oc} contours are almost identical, indicating that thickness has little effect and that the V_{oc} rises monotonically with N_A across the grid. The thickness effect is smaller than the N_A effect. Better band alignment/charge extraction and less recombination are consistent with the slight increase in V_{oc} with increasing N_A. The slight magnitude implies that the limited V_{oc} is caused by the N719 or other interfaces.

The change in J_{sc} as HTL thickness and doping density increase is depicted in Fig. 8 (b). While thickness and doping density varied simultaneously, the J_{sc} was attained in the 18.9077–19.4296 mA cm^{-2} range. Changes in thickness are much smaller than changes in N_A. The N_A is the determining factor. By improving hole extraction and lowering series resistance, raising the HTL N_A raises charge collection and, consequently, J_{sc}. The modest effect suggests that the HTL N_A collection efficiency fine-tuning controls the majority of photon absorption and generation. At 0.6 μm thickness and 10^{17} cm^{-3} N_A, the optical J_{sc} was detected.

The change in FF as HTL thickness and N_A increase is depicted in Fig. 8 (c). The thickness and doping density varied simultaneously, resulting in an FF that fell between 68.4488 and 68.5677%. The FF are tightly clustered, as can be seen (i.e. very small variation). The metric that is least affected by the monotonic increase of N_A is FF. The FF contour map displays a slight decline toward the high-thickness/high-N_A and a small local maximum at the thin edge (thickness = 0.1 μm) and at moderate N_A (~1×10^{18}). In another way, FF and N_A are not strictly monotonic. Although both are small in absolute terms, the average N_A effect (~0.116) is still greater than the thickness effect (~0.00999). Series resistance has an effect on the FF. Series resistance is decreased (FF is improved) by a thin HTL.

The contour plot of the PCE variation in relation to changes in HTL thickness and HTL N_A is displayed in Fig. 8 (d). At thickness = 0.6 μm and $N_A = 1 \times 10^{17}$, the efficiency was 11.28521% as the minimum, and at 0.6 μm and 1×10^{22} cm^{-3}, it was 11.60260% at the maximum. Between 0.1 and 0.6 μm, the efficiency is largely dependent on HTL N_A and hardly depends on thickness. In addition to improving hole conductivity and extraction, higher HTL N_A can decrease recombination at the HTL/N719 interface or increase built-in potential [16, 56].

3.6 Optimized performance

Following a thorough investigation on the different parameters of the studied layer, optimized values were obtained and further simulation was conducted to obtain the optimize device. The ETL thickness, dye thickness, ETL doping concentration, dye defect density, HTL thickness and doping concentration were optimized with values as shown Table 5. Utilizing the aforementioned parameters, a final optimized device was obtained with the following device performance; PCE = 23.75%, FF = 84.98% J_{sc} = 24.12 mA cm^{-2} and V_{oc} of 1.16 V. Fig. 9 (a) shows the *J-V* curve of both

Table 5 Optimized parameters of the device

Optimized parameters	ETL	Dye	HTL
Thickness (μm)	0.16	0.9	0.6
N_D (cm^{-3})	10^{20}	-	-
N_A (cm^{-3})	-	-	10^{22}
N_t (cm^{-2})	-	10^{13}	-

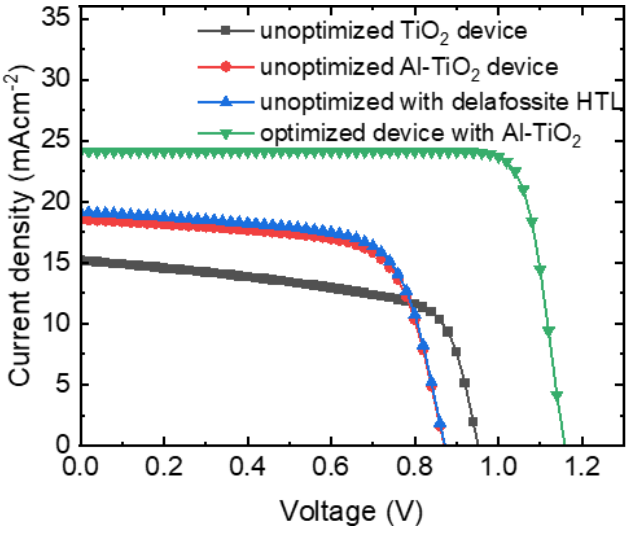

(a)

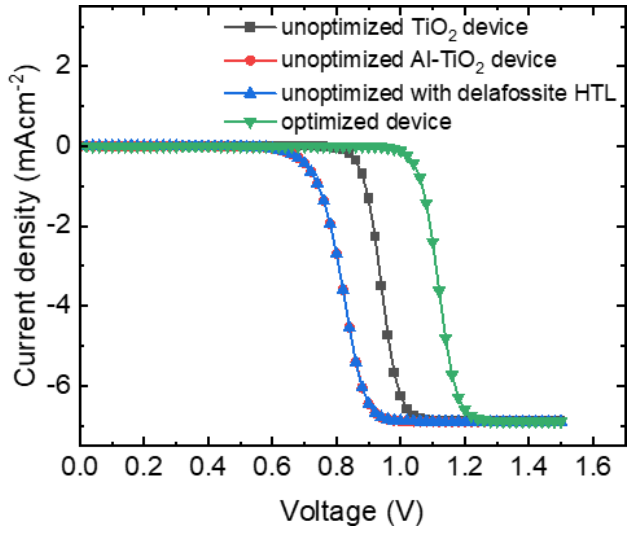

(b)

Fig. 9 (a) *J-V* curve with optimized and unoptimized data under illumination, and (b) *J-V* curve with optimized and unoptimized data under dark condition

optimized and unoptimized devices under illumination while Fig. 9 (b) shows the *J-V* curve of both optimized and unoptimized devices under dark condition.

3.7 Comparison of our SCAPS-1D results with other results previously reported

Table 6 [41, 43, 46, 47, 57–59] shows the comparison of previous studies (both experimental and simulated) with present study. All the experimental results are highly inferior as compared to the simulated ones. Previous simulation works showed that, there is much effort needed to realize a similar trademark documented for N719-based ssDSSCs. The optimized FTO/Al-TiO_2/N719/Mg-$CuCrO_2$/C structure shows an enhanced efficiency of PCE = 23.75%, supported with FF of 84.98% J_{sc} of 24.12 mA cm^{-2} and V_{oc} of 1.16 V. This study shows superior performance to previously reported data and has paved a new means to achieve better performance with dopant integration. It has also shown that proper charge transport channel and managed interfacial properties can greatly impact photovoltaic metrics. With enormous effort in efficiency management, proper charge transport selection and interface control, ssDSSC holds the potential to compete in viability of providing solution to the energy crisis.

3.8 Effect of metal back contact with different work function on the optimized device

From the property of the optimized device, the carbon-based metal back contact shows a PCE of 23.75%. Variation of work function (W_F) shows different photovoltaic performance [12, 16, 41, 48]. In Section 3.8, the impact of work function of metal contact was investigated. As indicated in Table 6 and Fig. 10. We have found that the V_{oc}, J_{sc}, FF, and PCE begin to increase as the W_F rises; hence, the observed trend was Cr < Mo < Fe < C < Au < W < Ni < Pd < Pt < Se. On close comparison, it was observed that same efficiency of 23.75% (see Table 7) were reported for Au, W, Ni, Pd, Pt, and Se back contacts. There was a decline in the performance with decrease in work function of metal contact. For example, the W_F of Cr as back contact was

Table 6 *J-V* data from present study and previously published literature

Configuration	Study	V_{oc} (V)	J_{sc} (mA cm^{-2})	FF (%)	PCE (%)	Remark
FTO/TiO_2/N719/CuSCN/C	Exp.	0.65	15.76	41.60	4.24	[46]
FTO/P-TiO_2/N719/CuSCN/G	Exp.	0.60	7.80	44.00	2.10	[47]
FTO/TiO_2/N719/CuI/Pt	Exp.	0.51	4.88	61.00	1.52	[57]
FTO/TiO_2/N719/PMII/Ir	Exp.	0.78	12.36	54.00	5.19	[58]
FTO/PCBM/N719/CuCSN/Au	Sim.	0.89	8.56	70.94	5.38	[43]
FTO/TiO_2/N719/CuSCN/Pt	Sim.	1.17	6.23	78.32	5.71	[41]
FTO/ZnOS/N719/CTZSe/Au	Sim.	0.87	20.83	70.86	12.91	[43]
FTO/TiO_2/N719/CuI/Au	Sim.	1.50	24.73	47.85	17.72	[59]
FTO/TiO_2/N719/CuSCN/Au	Sim.	1.20	24.58	56.71	16.69	[59]
FTO/TiO2/N719/spiro/Au	Sim.	0.99	22.58	53.74	12.20	[59]
FTO/Al-TiO2/N719/CuSCN/C	Sim.	1.16	24.12	84.98	23.75	[This work]

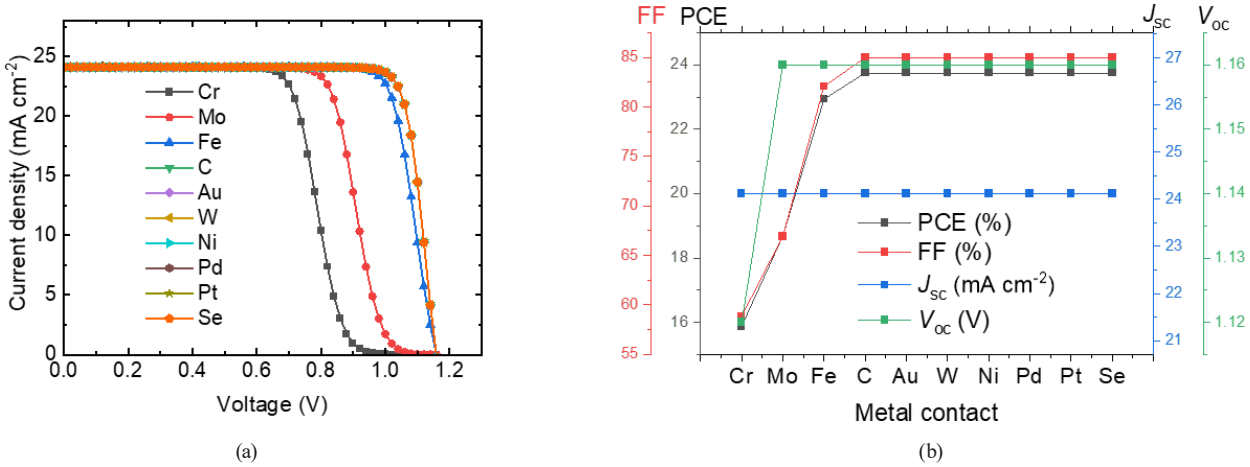

(a) (b)

Fig. 10 (a) *J-V* curve with various metal contact data, and (b) Variation of photovoltaic performance (PCE, FF, J_{sc} and V_{oc}) with various metal contact

Table 7 *J-V* parameters for various back-contact work functions

Metal contact	Work function (eV)	PCE (%)	FF (%)	J_{sc} (mA cm^{-2})	V_{oc} (V)
Cr	4.5	15.88	58.87	24.12	1.12
Mo	4.62	18.68	66.95	24.12	1.16
Fe	4.81	22.94	82.09	24.12	1.16
C	5.0	23.75	84.98	24.12	1.16
Au	5.1	23.75	84.99	24.12	1.16
W	5.22	23.75	84.99	24.12	1.16
Ni	5.5	23.75	84.99	24.12	1.16
Pd	5.6	23.75	84.99	24.12	1.16
Pt	5.7	23.75	84.99	24.12	1.16
Se	5.9	23.75	84.99	24.12	1.16

low, which results to its difficulties in moving to the surface of the metal, at the same time allowing easy flow of electrons. The high metric performance at higher metal W_F is attributed to the contact ability to weaken the Schottky barrier, favoring the transport of holes [12, 19, 48].

3.9 Effect of temperature on the optimized device

It is well known that temperature significantly affects solar cells metrics. The temperature was varied from 230 to 310 K at 10 K intervals to examine its effects on the optimized device. The current voltage curve for a range of temperatures is displayed in Fig. 11 (a). Fig. 11 (b) displays the dependence of the various metric parameters (PCE, FF, J_{sc}, and V_{oc}) on temperature. Variations in temperature have a significant impact on the device's photovoltaic performance (see Table 8). As the temperature rises, the V_{oc} and PCE decreases.

Equation (8) provides an approximation of a solar cell's open-circuit voltage V_{oc}:

$$V_{oc} = \frac{kT}{q}\ln\left(\frac{J_{sc}}{J_0}+1\right) \tag{8}$$

where k = Boltzmann constant, T = temperature, q = charge, J_{sc} = short circuit current density, J_0 = reverse saturation current density.

Higher carrier excitation across the band gap causes the reverse saturation current to increase exponentially with temperature. V_{oc} and PCE decreases as a result of the increased recombination rate brought on by this increase in saturation current [22, 56]. As the temperature increases, charge carriers gain more thermal energy, which causes momentum loss and scattering to increase. This increases the likelihood of recombination. Moreover, additional non-radiative recombination centers that can be triggered by high temperatures include defects or trap states in the material. These centers increase the overall recombination rate and reduce the percentage of radiative recombination by providing alternative pathways for carrier recombination without photon emission [16, 50]. Changes in device resistance occur with increasing temperature, affecting electron and hole mobilities, carrier concentrations, and ultimately the fill factor. The fill factor drops between 230 and 250 K because low temperature carrier mobility results

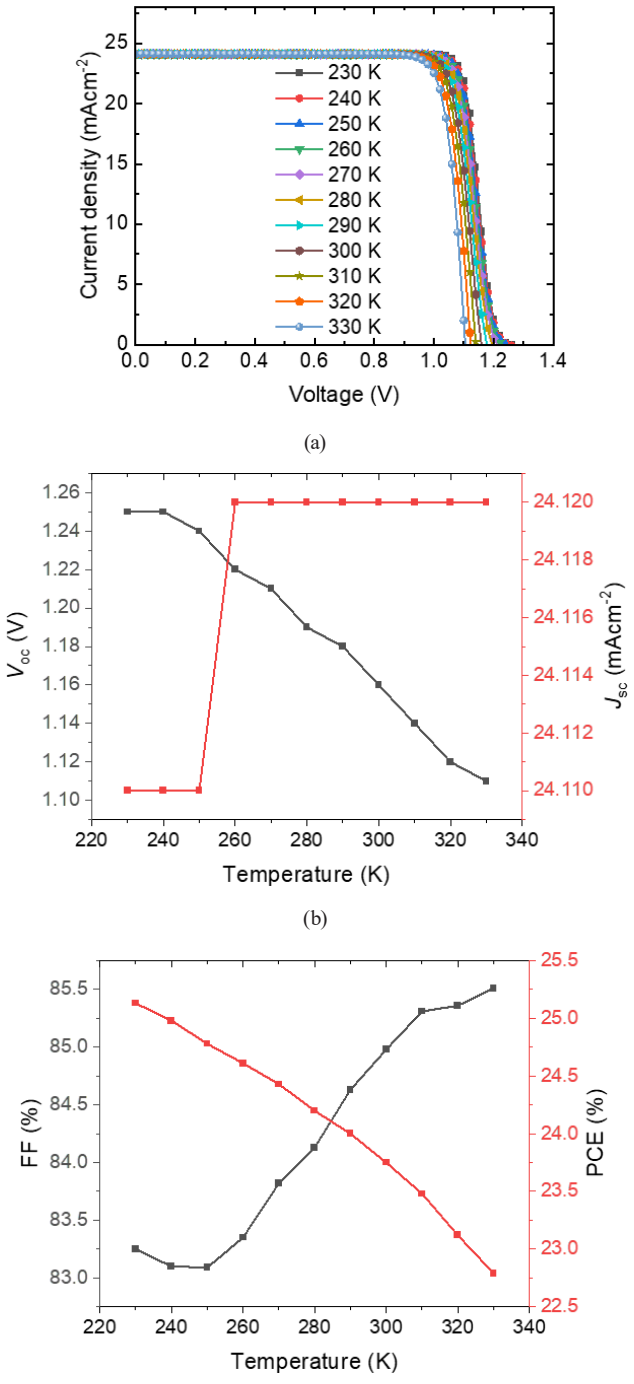

Fig. 11 (a) *J-V* curve with varied thickness, (b) J_{sc} and V_{oc} (c) PCE and FF with temperature

Table 8 *J-V* characteristics at various operating temperatures

Temperature	V_{oc} (V)	J_{sc} (mA cm^{-2})	FF (%)	PCE (%)
230	1.25	24.11	83.25	25.13
240	1.25	24.11	83.10	24.98
250	1.24	24.11	83.09	24.78
260	1.22	24.12	83.35	24.61
270	1.21	24.12	83.82	24.43
280	1.19	24.12	84.13	24.20
290	1.18	24.12	84.63	24.00
300	1.16	24.12	84.98	23.75
310	1.14	24.12	85.31	23.48
320	1.12	24.12	85.36	23.12
330	1.11	24.12	85.51	22.79

in increased series resistance and ineffective charge transport, which impairs the device's capacity to deliver power effectively [44]. Thermal activation increases carrier mobility and conductivity as the temperature rises from roughly 260 K to 330 K [44, 56]. This lowers resistive losses and improves charge extraction. Over this higher temperature range, the fill factor gradually recovers and rises as a result of the enhanced transport outweighing the increased recombination [48]. Because band gap narrowing increases photon absorption, the short-circuit current may slightly increase as the temperature rises, but this effect is negligible in comparison to the significant decrease in V_{oc}.

3.10 Series resistance on the optimized device

The performance of ssDSSC is highly influenced by series resistance (R_S). The series resistance is made up of the ohmic contact and the active layer resistance, which can be affected by the flow of current through the solar cell's interfaces [10, 56]. The behavior of ssDSSC at different R_S is controlled by Eq. (9) [10]. Study have shown that at high series resistance, the performance of ssDSSC device is low [16].

$$J_{sc} = J_{PH} - J_0\left[\exp\left(\frac{q\left(V - JR_S\right)}{nkT_e}\right) - 1\right] - \frac{V - JR_S}{R_{sh}} \tag{9}$$

Where q represents the charge, J_{PH} denotes the current density, J_0 stands for reverse bias saturation current, the series resistance is R_S, R_{sh} stands for the shunt resistance, the diode ideality factor is n, the Boltzmann constant is k and T_e is the ambient temperature.

Three factors basically affect the series resistance of our simulated solar cell, which are; current flow at the ETL/N719 and N719/HTL interfaces, the back/FTO interface and lastly, the front and back contact resistances [60]. Through device doping, the R_S can be managed to give improved conductivity [61]. During the simulation of the device, the series resistance was varied from 0 to 6 Ω cm^2 to explore their influence on the output of the device while having a fixed shunt resistance of 10^6 Ω cm^2. Fig. 12 (a), (b) presents the current-voltage plot and power-voltage of the device with various R_S value. The relationship between the FF, PCE, V_{oc} and J_{sc} at different R_S is depicted in Fig. 13 (a)–(d). Table 9 shows decrease in PCE and FF as R_S increases. Same patterns have been reported in previous research [8, 16, 56, 62]. As series resistance increases, more voltage losses are introduced into the device when current flows, which lowers the solar cell's PCE and FF. The actual voltage available at the external terminals is decreased by this resistance, which comes from the bulk layers, interfaces, and contacts [56].

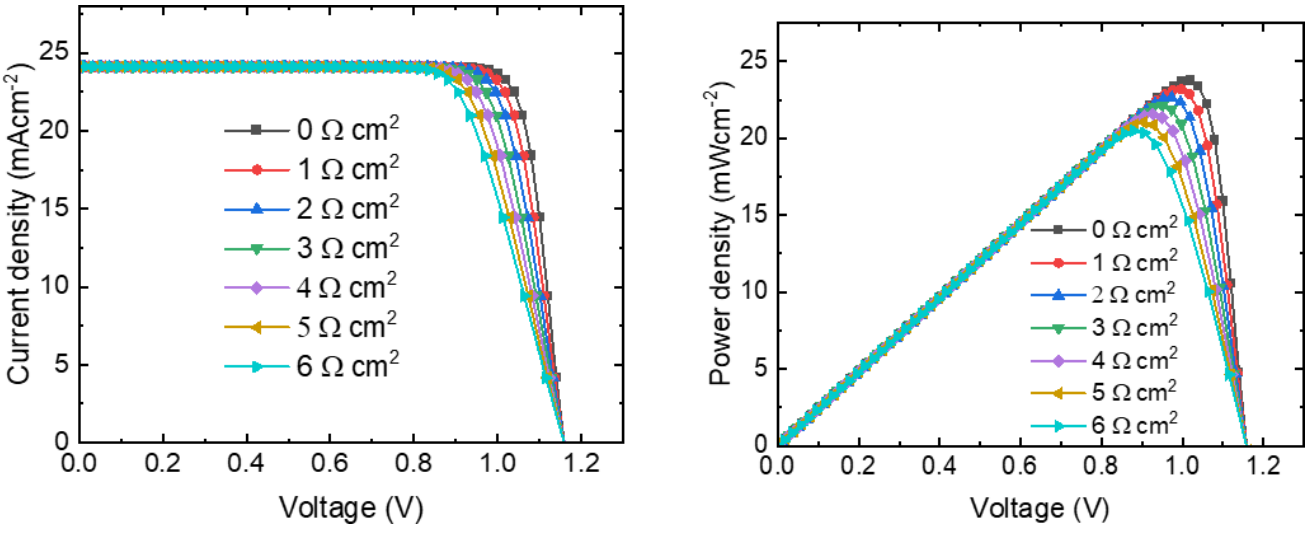

(a) (b)

Fig. 12 (a) *J-V* curve with various R_S and (b) *P-V* curve with various R_S

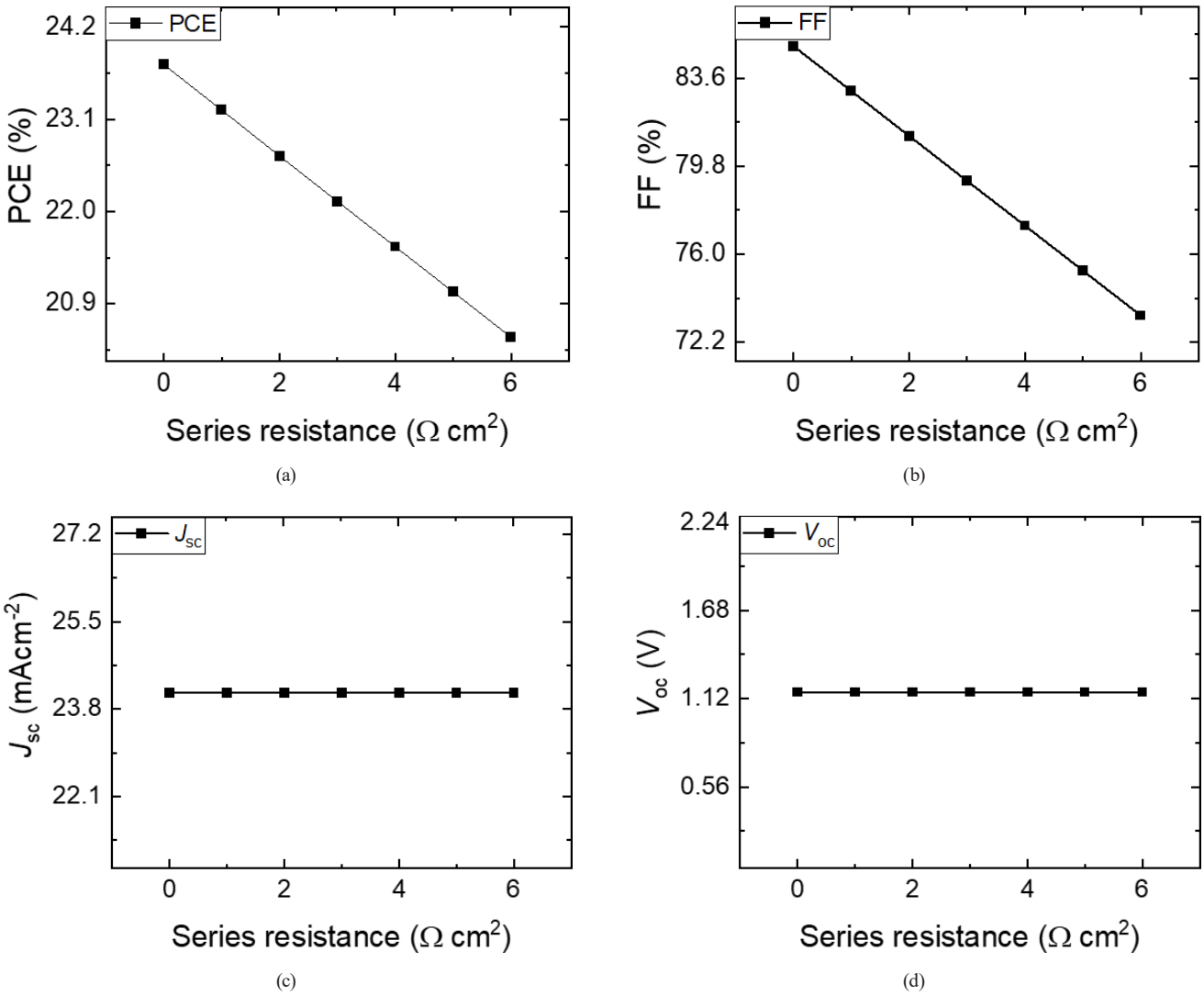

Fig. 13 Correlation between (a) PCE, (b) FF, (c) J_{sc} and (d) V_{oc} with R_S

Table 9 *P-V* metrics data with varied R_S

R_S (Ω cm²)	PCE (%)	FF (%)	J_{sc} (mA cm⁻²)	V_{oc} (V)
0	23.75	84.98	24.12	1.16
1	23.21	83.04	24.12	1.16
2	22.66	81.10	24.12	1.16
3	22.12	79.16	24.12	1.16
4	21.58	77.23	24.12	1.16
5	21.04	75.29	24.12	1.16
6	20.50	73.35	24.12	1.16

Consequently, the fill factor decreases as the squareness of the *J-V* curve becomes less. Series resistance reduces the fill factor, which in turn lowers the overall power conversion efficiency. The rise in R_S values have no appreciable effect on J_{sc} and V_{oc}. Since the V_{oc} and J_{sc} are measured when the current flowing through the device is either zero (for V_{oc}) or zero (for J_{sc}), they are largely unaffected by an increase in series resistance. Since there is no current flowing at V_{oc}, there is very little internal voltage drop across the resistance; at J_{sc}, on the other hand, there is no external voltage, so the series resistance has no effect on the extracted current [63].

3.11 Effect of shunt resistance on the optimized device

The performance of PSC is highly influenced by shunt resistance R_{sh}. The function of losses due to current leakages and recombination of free electrons and holes is termed as shunt resistance [64]. The behavior of ssDSSC at different R_S is controlled by Eqs. (9) and (10) [10].

$$V_{oc} = \left(\frac{nkT_e}{q_e}\right) \ln\left\{\frac{J_{PH}}{J_0}\left(1 - \frac{V_{oc}}{J_{PH}R_{sh}}\right)\right\} \tag{10}$$

During the simulation of the device, the shunt resistance was varied from 10^1 to 10^7 Ω cm^2 to explore their influence on the output of the device while having a fixed series resistance of 0 Ω cm^2. Fig. 14 (a)–(d) shows the relationship between the FF, PCE, V_{oc} and J_{sc} at different R_{sh} values. It can be shown from the values that increasing the R_{sh} value, brings about increase in PCE and FF from 1.45 to 23.75% and 15.00 to 84.98% (see Table 10).

At R_{sh} values of 10^6 and 10^7 Ω cm^2 the PCE and FF remained unchanged. At low R_{sh} values, the performance became inferior due to bypassing of significant leakage currents in the external circuit that create power loss. As a result, photovoltaic performance deteriorates, which lowers overall efficiency. Since leakage currents reduce the total potential difference between the cell terminals, low R_{sh} results in a decrease in V_{oc} [16, 56]. Significant current loss, particularly close to the maximum power point, is caused by low shunt resistance, flattening the *J-V* curve and lowering FF. These leakage currents are inhibited by high shunt resistance, maintaining the solar cell's optimal diode behavior [8, 23]. Because efficiency is directly proportional to FF, this leads to a more squared *J-V* curve with improved FF, and the PCE rises in tandem. The J_{sc} remains constant as shunt resistance increases. Since J_{sc} is measured at zero applied voltage, where the impact of leakage paths is negligible, at this stage, light absorption and carrier collection determine the photocurrent instead of resistive losses.

3.12 Effect of capacitance and Mott−Schottky analysis

The built-in potential (V_{bi}), which results from the potential difference created at the semiconductor junction, drives photogenerated charge carriers in semiconductors

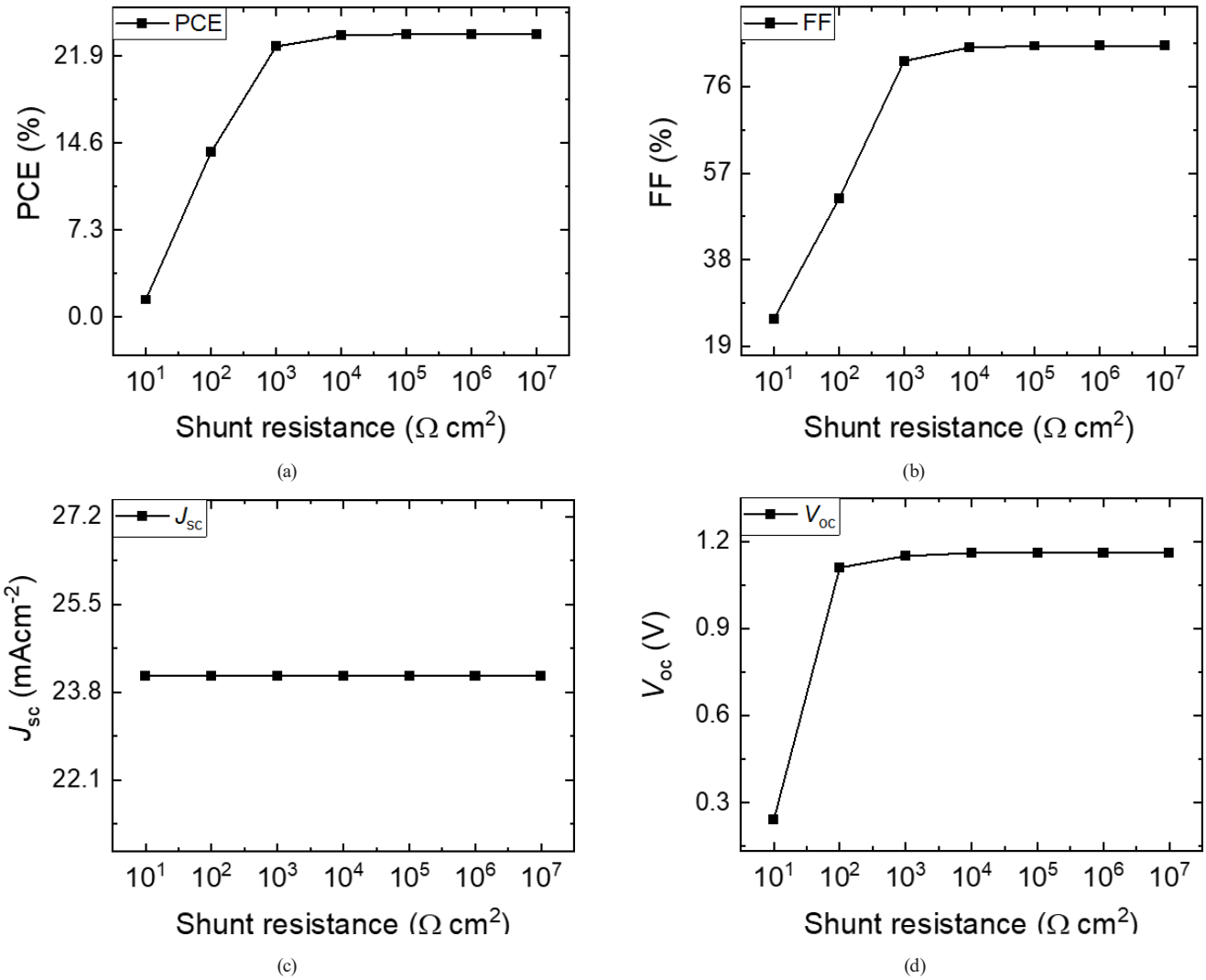

Fig. 14 Correlation between (a) PCE, (b) FF, (c) J_{sc} and (d) V_{oc} with R_{sh}

Table 10 PV metrics data with varied R_s

R_{sh} (Ω cm^2)	PCE (%)	FF (%)	J_{sc} (mA cm^{-2})	V_{oc} (V)
10^1	1.45	25.00	24.12	0.24
10^2	13.82	51.45	24.12	1.11
10^3	22.71	81.65	24.12	1.15
10^4	23.64	84.65	24.12	1.16
10^5	23.74	84.95	24.12	1.16
10^6	23.75	84.98	24.12	1.16
10^7	23.75	84.98	24.12	1.16

in opposite directions [65]. The main determining factor for good PCE in solar cell is the V_{bi}, which functions by simply reducing the possibility of bulk and interface recombination, along with minimal carrier accumulation. It attained its value at the Mott-Schottky capacitance calculation. The interface between ETL and front contact has been considered as Schottky contact [33]. The rise in capacitance (C) is caused by the space charge region which lowers the built-in potential. The capacitance can attain even a negative value at specific voltage wave [66]. This Mott-Schottky calculation is considered a pronounce path for obtaining concentration of charge carrier as shown in Eq. (11) [67]:

$$\frac{1}{C^2} = \frac{2}{S^2 \times \varepsilon} \times \frac{1}{qN_A}\left(V - V_{bi} - \frac{k_b T}{q}\right) \tag{11}$$

where the surface area is S.

Fig. 15 (a) depicts the dependence of the capacitance with temperature, while Fig. 15 (b) shows the Mott-Schottky plot with dependence at voltage range of −0.8 to 0.8 V and stable frequency of 10^6 Hz. It has been found that, increase in temperature decreases the capacitance gradually. This means that rising the temperature results to higher recombination rate and enhanced series resistance. While the device at 310 K shows a capacitance value of 10.62 nF cm^{-2}, other capacitances ranged between 2.10 to 6.23 nF cm^{-2}, with 2.10 nF cm^{-2} for device at 350 K, 2.68 nF cm^{-2} for device at 340 K, 3.95 nF cm^{-2} for device at 330 K and 6.23 nF cm^{-2} for device at 320 K. The Mott-Schottky plot shows the device at 350 K to have the highest value with that at 310 K having the lowest value. This estimation can be used to predict the built-in potential.

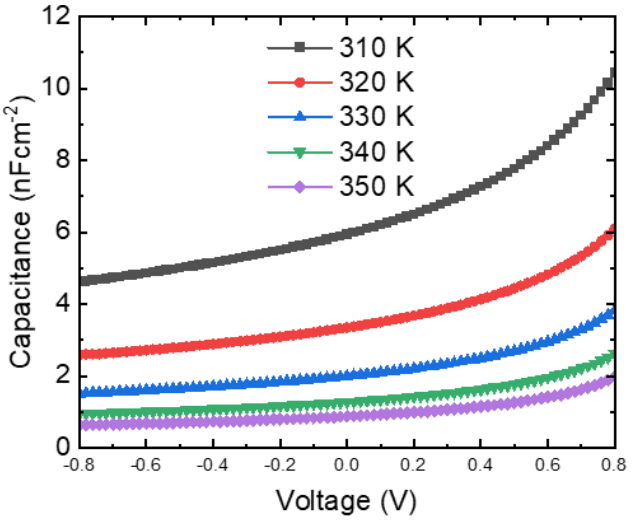

(a)

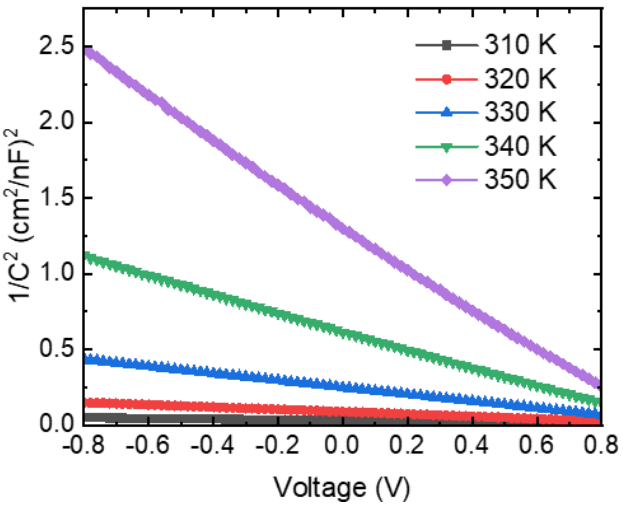

(b)

Fig. 15 (a) C-V characteristics as a function of varied temperature, (b) Mott-Schottky plot

4 Conclusion

The photovoltaic performance of ssDSSCs with the configuration FTO/ETL/N719/HTL/C was systematically investigated in this work. The initial evaluation with the structure FTO/TiO_2/N719/CuSCN/C demonstrated a PCE of 0.95 V, 15.16 mA cm^{-2}, 64.49% and 9.30%. The results with the configuration device FTO/Al-TiO_2/N719/CuCSN/C presents 0.87 V, 18.53 mA cm^{-2}, 68.73% and 11.09% as V_{oc}, J_{sc}, FF and PCE which shows that the device with Al-TiO_2 ETL is more superior. Optimizing different HTLs (CuSCN, CuO, Cu_2O, $CuSbS_2$, $CuCrO_2$ and Mg-$CuCrO_2$), shows the order of PCE as Mg-$CuCrO_2$ (11.44%) > $CuCrO_2$ (11.24%) > CuSCN (11.09%) > CuO (9.77%) > Cu_2O (8.63%) > $CuSbS_2$ (5.87%). The ETL thickness and doping concentration, dye thickness and defect density, and HTL thickness and doping concentration optimization on the FTO/Al-TiO_2/N719/Mg-$CuCrO_2$/C configuration shows optimal values of 0.16 µm, 10^{20} cm^{-3}, 0.9 µm, 10^{13} cm^{-2}, 0.6 µm and

10^{22} cm^{-3}, respectively. The simulation with these optimal values gave a PCE = 23.75%, supported with FF of 84.98% J_{sc} of 24.12 mA cm^{-2} and V_{oc} of 1.16 V. The effect of series and shunt resistance, temperature, metal work function, capacitance and Mott-Schottky analysis were also studied. The results show consistency with basic equations. It was also found that, the PCE decreases with increase in temperature. The Mott-Schottky results presents a deeper knowledge in the underlying mechanism governing solar cell operation. This work holds the potential to provide new scientific knowledge for cleaner production strategies in industries utilizing dye materials for the broader field of energy, ultimately contributing to the reduction of carbon footprint.

Conflict of interest

Authors have declared that there was no conflict of interest.

Data availability statement

The data that support this paper will be made available upon reasonable request.

Acknowledgement

The authors would like to thank Professor Marc Burgelman and his team from the Department of Electronics and Information Systems, University of Ghent, Belgium, for the development of the SCAPS software package and allowing its use.

Funding

Funding for this research was supported by the Central Postdoctoral Fellowship Funding at Central University of Technology, Free State, South Africa.

References

[1] Holechek, J. L., Geli, H. M. E., Sawalhah, M. N., Valdez, R. "A Global Assessment: Can Renewable Energy Replace Fossil Fuels by 2050?", Sustainability, 14(8), 4792, 2022. https://doi.org/10.3390/su14084792

[2] Chanchangi, Y. N., Adu, F., Ghosh, A., Sundaram, S., Mallick, T. K. "Nigeria's energy review: Focusing on solar energy potential and penetration", Environment, Development and Sustainability, 25(7), pp. 5755–5796, 2023. https://doi.org/10.1007/s10668-022-02308-4

[3] Kurokawa, Y., Kato, T., Pandey, S. S. "Fabrication of Solid-State Dye-Sensitized Solar Cells by Controlled Evaporation of Solvents for Creation of Facile Charge Transport Pathway", Physica Status Solidi (a) Applications and Materials Science, 220(24), 2300116, 2023. https://doi.org/10.1002/pssa.202300116

[4] Yadagiri, B., Kumar Kaliamurthy, A., Yoo, K., Cheol Kang, H., Ryu, J., Kwaku Asiam, F., Lee, J.-J. "Molecular Engineering of Photosensitizers for Solid-State Dye-Sensitized Solar Cells: Recent Developments and Perspectives", ChemistryOpen, 12(12), e202300170, 2023. https://doi.org/10.1002/open.202300170

[5] Danladi, E., Oguzie, E. E., Ezema, F. I. "Challenges and outlooks on stability of inverted perovskite solar cells: a review insight", Multiscale and Multidisciplinary Modeling, Experiments and Design, 8(1), 119, 2025. https://doi.org/10.1007/s41939-024-00699-7

[6] Danladi, E., Mutah, W., Jubu, P. R., Ogunmoye, K. A., Abubakar, Z. L., …, Ezema, F. "Photovoltaic Performance of $CsPbBr_3$-based Perovskite Solar Cell with TiO_2 and Quarternary Chalcogenide Cu_2FeSnS_4 as Charge Transport Channels: Unlocking >26% Efficiency via SCAPS-1D Investigation", Next Energy, 9, 100423, 2025. https://doi.org/10.1016/j.nxener.2025.100423

[7] Danladi, E., Ichoja, A., Onoja, E. D., Adepehin, D. S., Onwoke, E. E., Ekwu, O. M., Alfred, D. O. "Broad-band-enhanced and minimal hysteresis perovskite solar cells with interfacial coating of biogenic plasmonic light trapping silver nanoparticles", Materials Research Innovations, 27(7), pp. 521–536, 2023. https://doi.org/10.1080/14328917.2023.2204585

[8] Danladi, E., Obagboye, L. F., Aisida, S., Ezema, F. I., Okorie, O., Bwamba, J. A., Emmanuel, P. A., Hussaini, A. A., Jubu, P. R., Ozurumba, A. C. "20.730% highly efficient lead-free $CsSnI_3$-based perovskite solar cells with various charge transport materials: a SCAPS-1D study", Multiscale and Multidisciplinary Modeling, Experiments and Design, 8(1), 114, 2025. https://doi.org/10.1007/s41939-024-00701-2

[9] Bolarinwa, S. O., Danladi, E., Ichoja, A., Onimisi, M. Y., Achem, C. U. "Synergistic Study of Reduced Graphene Oxide as Interfacial Buffer Layer in HTL-free Perovskite Solar Cells with Carbon Electrode", Journal of the Nigerian Society of Physical Sciences, 4(3), 909, 2022. https://doi.org/10.46481/jnsps.2022.909

[10] Danladi, E., Oguzie, E. E., Ezema, F. I. "Highly efficient 25.562% $Cs_2AgBiBr_6$ double perovskite solar cell with copper barium tin sulfide and ZnO as charge transport channels: an intuition from a theoretical study using SCAPS-1D", Journal of Photonics for Energy, 15(2), 024501, 2025. https://doi.org/10.1117/1.JPE.15.024501

[11] Nyiekaa, E. A., Aika, T. A., Orukpe, P. E., Akhabue, C. E., Danladi, E. "Development on inverted perovskite solar cells: A review", Heliyon, 10(2), e24689, 2024. https://doi.org/10.1016/j.heliyon.2024.e24689

[12] Durodola, O. M., Ugwu, C., Danladi, E. "Highly efficient lead-free perovskite solar cell based on magnesium-doped copper delafossite hole transport layer: a SCAPS-1D framework prospect", Emergent Materials, 6(5), pp. 1665–1684, 2023. https://doi.org/10.1007/s42247-023-00542-8

[13] Sharma, R., Sharma, A., Agarwal, S., Dhaka, M. S. "Stability and efficiency issues, solutions and advancements in perovskite solar cells: A review", Solar Energy, 244, pp. 516–535, 2022. https://doi.org/10.1016/j.solener.2022.08.001

[14] Benesperi, I., Michaels, H., Freitag, M. "The researcher's guide to solid-state dye-sensitized solar cells", Journal of Materials Chemistry C, 6(44), pp. 11903–11942, 2018. https://doi.org/10.1039/C8TC03542C

[15] Cao, Y., Saygili, Y., Ummadisingu, A., Teuscher, J., Luo, J., …, Grätzel, M. "11% efficiency solid-state dye-sensitized solar cells with copper(II/I) hole transport materials", Nature Commununications, 8(1), 15390, 2017. https://doi.org/10.1038/ncomms15390

[16] Tariq, M. U. N., Masud, M. I., Dmour, H. A., Ghulman, H. A., Kashif, M., Malik, M., Nahas, M. "Optimization of high-efficiency solid-state dye sensitized solar cells (ssDSSCs) based on N719 dye via electron transport layer engineering using SCAPS-1D", Results in Engineering, 27, 106465, 2025. https://doi.org/10.1016/j.rineng.2025.106465

[17] Danladi, E., Jubu, P. R., Tighezza, A. M., Hossain, I., Tasie, N. N., …, Amanyi, M. I. "Highly efficient, hole transport layer (HTL)-free perovskite solar cell based on lithium-doped electron transport layer by device simulation", Emergent Materials, 6(6), pp. 1779–1795, 2023. https://doi.org/10.1007/s42247-023-00558-0

[18] Uddin, M. S., Hossain, M. K., Uddin, M. B., Toki, G. F. I., Ouladsmane, M., Rubel, M. H. K., Tishkevich, D. I., Sasikumar, P., Haldhar, R., Pandey, R. "An In-Depth Investigation of the Combined Optoelectronic and Photovoltaic Properties of Lead-Free $Cs_2AgBiBr_6$ Double Perovskite Solar Cells Using DFT and SCAPS-1D Frameworks", Advanced Electronic Materials, 10(5), 2300751, 2024. https://doi.org/10.1002/aelm.202300751

[19] Hossain, M. K., Toki, G. F. I., Alam, I., Pandey, R., Samajdar, D. P., …, Mohammed, M. K. A. "Numerical simulation and optimization of a $CsPbI_3$-based perovskite solar cell to enhance the power conversion efficiency", New Journal of Chemistry, 47(10), pp. 4801–4817, 2023. https://doi.org/10.1039/D2NJ06206B

[20] Rafique, M., Hajra, S., Irshad, M., Usman, M., Imran, M., Assiri, M. A., Ashraf, W. M. "Hydrogen Production Using TiO_2-Based Photocatalysts: A Comprehensive Review", ACS Omega, 8(29), pp. 25640–25648, 2023. https://doi.org/10.1021/acsomega.3c00963

[21] Thabet, S. M., Abdelhamid, H. N., Ibrahim, S. A., El-Bery, H. M. "Boosting photocatalytic water splitting of TiO_2 using metal (Ru, Co, or Ni) co-catalysts for hydrogen generation", Scientific Reports, 14(1), 10115, 2024. https://doi.org/10.1038/s41598-024-59608-0

[22] Hossain, M. K., Ishraque Toki, G. F., Samajdar, D. P., Rubel, M. H. K., Mushtaq, M., …, Madan, J. "Photovoltaic Performance Investigation of $Cs_3Bi_2I_9$-Based Perovskite Solar Cells with Various Charge Transport Channels Using DFT and SCAPS-1D Frameworks", Energy & Fuels, 37(10), pp. 7380–7400, 2023. https://doi.org/10.1021/acs.energyfuels.3c00540

[23] Usman, A., Bovornratanaraks, T. "Modeling and Optimization of Modified TiO_2 with Aluminum and Magnesium as ETL in $MAPbI_3$ Perovskite Solar Cells: SCAPS 1D Frameworks", ACS Omega, 9(38), pp. 39663–39672, 2024. https://doi.org/10.1021/acsomega.4c04505

[24] Rafieh, A. I., Ekanayake, P., Wakamiya, A., Nakajima, H., Lim, C. M. "Enhanced performance of $CH_3NH_3PbI_3$-based perovskite solar cells by tuning the electrical and structural properties of mesoporous TiO_2 layer via Al and Mg doping", Solar Energy, 177, pp. 374–381, 2019. https://doi.org/10.1016/j.solener.2018.11.024

[25] Lan, C., Luo, J., Lan, H., Fan, B., Peng, H., Zhao, J., Sun, H., Zheng, Z., Liang, G., Fan, P. "Enhanced charge extraction of Li-doped TiO_2 for efficient thermal-evaporated Sb_2S_3 thin film solar cells", Materials, 11(3), 355, 2018. https://doi.org/10.3390/ma11030355

[26] Giordano, F., Abate, A., Correa Baena, J. P., Saliba, M., Matsui, T., Im, S. H., Zakeeruddin, S. M., Nazeeruddin, M. K., Hagfeldt, A., Graetzel, M. "Enhanced electronic properties in mesoporous TiO_2 via lithium doping for high-efficiency perovskite solar cells", Nature Communication, 7(1), 10379, 2016. https://doi.org/10.1038/ncomms10379

[27] Vlachopoulos, N., Grätzel, M., Hagfeldt, A. "Solid-state dye-sensitized solar cells using polymeric hole conductors", RSC Advances, 11(62), pp. 39570–39581, 2021. https://doi.org/10.1039/D1RA05911D

[28] Li, S., Cao, Y.-L., Li, W.-H., Bo, Z.-S. "A brief review of hole transporting materials commonly used in perovskite solar cells", Rare Metals, 40(10), pp. 2712–2729, 2021. https://doi.org/10.1007/s12598-020-01691-z

[29] Hossain, M. K., Toki, G. F. I., Kuddus, A., Rubel, M. H. K., Hossain, M. M., Bencherif, H., Rahman, M. F., Islam, M. R., Mushtaq, M. "An extensive study on multiple ETL and HTL layers to design and simulation of high-performance lead-free $CsSnCl_3$-based perovskite solar cells", Scientific Reports, 13(1), 2521, 2023. https://doi.org/10.1038/s41598-023-28506-2

[30] Sarker, S., Islam, M. T., Rauf, A., Al Jame, H., Jani, M. R., Ahsan, S., Islam, M. S., Nishat, S. S., Shorowordi, K. M., Ahmed, S. "A SCAPS simulation investigation of non-toxic $MAGeI_3$-on-Si tandem solar device utilizing monolithically integrated (2-T) and mechanically stacked (4-T) configurations", Solar Energy, 225, pp. 471–485, 2021. https://doi.org/10.1016/j.solener.2021.07.057

[31] Chen, J., Park, N.-G. "Inorganic Hole Transporting Materials for Stable and High Efficiency Perovskite Solar Cells", The Journal of Physical Chemistry C, 122(25), pp. 14039–14063, 2018. https://doi.org/10.1021/acs.jpcc.8b01177

[32] Cetin, C., Chen, P., Hao, M., He, D., Bai, Y., Lyu, M., Yun, J.-H., Wang, L. "Inorganic p-Type Semiconductors as Hole Conductor Building Blocks for Robust Perovskite Solar Cells", Advanced Sustainable Systems, 2(8–9), 1800032, 2018. https://doi.org/10.1002/adsu.201800032

[33] Sarkar, D. K., Mahmud Hasan, A. K., Mottakin, M., Selvanathan, V., Sobayel, K., ..., Akhtaruzzaman, M. "Lead free efficient perovskite solar cell device Optimization and defect study using Mg doped $CuCrO_2$ as HTL and WO_3 as ETL", Solar Energy, 243, pp. 215–224, 2022. https://doi.org/10.1016/j.solener.2022.07.013

[34] Wang, J., Zheng, P., Zhou, X., Fang, L. "Investigation of structural, morphological, optical, and electrical properties of $CuCrO_2$ films prepared by sol–gel method", Journal of Sol-Gel Science and Technology, 79(1), pp. 37–43, 2016. https://doi.org/10.1007/s10971-016-4003-6

[35] Bai, Z., Chen, S.-C., Lin, S.-S., Shi, Q., Lu, Y.-B., Song, S.-M., Sun, H. "Review in optoelectronic properties of p-type $CuCrO_2$ transparent conductive films", Surfaces and Interfaces, 22, 100824, 2021. https://doi.org/10.1016/j.surfin.2020.100824

[36] Jeong, S., Seo, S., Shin, H. "p-Type $CuCrO_2$ particulate films as the hole transporting layer for $CH_3NH_3PbI_3$ perovskite solar cells", RSC Advances, 8(49), pp. 27956–27962, 2018. https://doi.org/10.1039/C8RA02556H

[37] University of Gent "SCAPS-1D, (3.3.10)", [computer program] Available at: https://scaps.elis.ugent.be/ [Accessed: 13 September 2025]

[38] Kowsar, A., Debnath, S. C., Shafayet-Ul-Islam, M., Hossain, M. J., Hossain, M., Chowdhury, A. K., Hashmi, G., Farhad, S. F. U. "An overview of solar cell simulation tools", Solar Energy Advances, 5, 100077, 2025. https://doi.org/10.1016/j.seja.2024.100077

[39] Burgelman, M., Decock, K., Niemegeers, A., Verschraegen, J., Degrave, S. "SCAPS Manual", University of Gent, Gent, Belgium, 2025.

[40] Saidarsan, A., Guruprasad, S., Malik, A., Basumatary, P., Ghosh, D. S. "A critical review of unrealistic results in SCAPS-1D simulations: Causes, practical solutions and roadmap ahead", Solar Energy Materials and Solar Cells, 279, 113230, 2025. https://doi.org/10.1016/j.solmat.2024.113230

[41] Danladi, E., Kashif, M., Daniel, T., Achem, C., Alpha, M., Gyan, M. "7.379% Power Conversion Efficiency of a Numerically Simulated Solid State Dye Sensitized Solar Cell With Copper (I) Thiocyanate as a Hole Conductor", East European Journal of Physics, 3, pp. 19–31, 2022. https://doi.org/10.26565/2312-4334-2022-3-03

[42] Deepak, K., Sharath Chandra Reddy, G., Tiwari, C. "Performance Analysis of SnO_2/$CsSnGeI_3$/CuSCN perovskite solar cells using SCAPS 1D Simulator", Journal of Physics: Conference Series, 2571(1), 012023, 2023. https://doi.org/10.1088/1742-6596/2571/1/012023

[43] Korir, B. K., Kibet, J. K., Ngari, S. M. "Simulated performance of a novel solid-state dye-sensitized solar cell based on phenyl-C_{61}-butyric acid methyl ester ($PC_{61}BM$) electron transport layer", Optical and Quantum Electronics, 53(7), 368, 2021. https://doi.org/10.1007/s11082-021-03013-8

[44] Danladi, E., Koao, L. F., Motaung, T. E., Usman, A., Motloung, S. V. "Unveiling the potential of $Cs_2AgBiBr_6$ double perovskite solar cells: a detailed study of the optoelectronic and photovoltaic properties via DFT and SCAPS-1D frameworks", 100(12), 125936, 2025. https://doi.org/10.1088/1402-4896/ae298d

[45] Ozurumba, A. C., Ogueke, N. V., Madu, C. A., Danladi, E., Mbachu, C. P., Yusuf, A. S., Gyuk, P. M., Hossain, I. "SCAPS-1D simulated organometallic halide perovskites: A comparison of performance under Sub-Saharan temperature condition", Heliyon, 10(8), e29599, 2024. https://doi.org/10.1016/j.heliyon.2024.e29599

[46] Premalal, E. V. A., Dematage, N., Konno, A. "Carbon black paste combined with conductivity-enhanced CuSCN for improved performance in quasi-solid-state dye-sensitized solar cells", Chemistry Letters, 41(5), pp. 510–512, 2012. https://doi.org/10.1246/cl.2012.510

[47] O'Regan, B., Lenzmann, F., Muis, R., Wienke, J. "A solid-state dye-sensitized solar cell fabricated with pressure-treated P25-TiO_2 and CuSCN: Analysis of pore filling and IV characteristics", Chemistry of Materials, 14(12), pp. 5023–5029, 2002. https://doi.org/10.1021/cm020572d

[48] Danladi, E., Gyuk, P. M., Tasie, N. N., Egbugha, A. C., Behera, D., Hossain, I., Bagudo, I. M., Madugu, M. L., Ikyumbur, J. T. "Impact of hole transport material on perovskite solar cells with different metal electrode: A SCAPS-1D simulation insight", Heliyon, 9(6), e16838, 2023. https://doi.org/10.1016/j.heliyon.2023.e16838

[49] Pindolia, G., Shinde, S. M., Jha, P. K. "Optimization of an inorganic lead free $RbGeI_3$ based perovskite solar cell by SCAPS-1D simulation", Solar Energy, 236, pp. 802–821, 2022. https://doi.org/10.1016/j.solener.2022.03.053

[50] Kenfack, A. D. K., Msimanga, M. "Effect of low-cost hole transport layers (HTLs) on the performance parameters of lead-free homojunction $CsGeI_2Br$-based perovskite solar cells", Next Materials, 6, 100482, 2025. https://doi.org/10.1016/j.nxmate.2024.100482

[51] Braun, S., Salaneck, W. R., Fahlman, M. "Energy-level alignment at organic/metal and organic/organic interfaces", Advanced Materials, 21(14–15), pp. 1450–1472, 2009. https://doi.org/10.1002/adma.200802893

[52] Srivastava, A., Kasliwal, M., Shirage, P. M. "From HTL to HTL-free: Experimental and numerically modelled performance dynamics of $Cs_2AgBiBr_6$ double perovskite solar cells", Solar Energy, 298, 113733, 2025. https://doi.org/10.1016/j.solener.2025.113733

[53] Aghazada, S., Nazeeruddin, M. K. "Ruthenium complexes as sensitizers in dye-sensitized solar cells", Inorganics, 6(2), 52, 2018. https://doi.org/10.3390/inorganics6020052

[54] Mosconi, E., Selloni, A., De Angelis, F. "Solvent effects on the adsorption geometry and electronic structure of dye-sensitized TiO_2: A first-principles investigation", The Journal of Physical Chemistry C, 116(9), pp. 5332–5340, 2012. https://doi.org/10.1021/jp209420h

[55] Sharma, K., Sharma, V., Sharma, S. S. "Dye-Sensitized Solar Cells: Fundamentals and Current Status", Nanoscale Research Letters, 13(1), 381, 2018. https://doi.org/10.1186/s11671-018-2760-6

[56] Danladi, E., Egbugha, A. C., Obasi, R. C., Tasie, N. N., Achem, C. U., Haruna, I. S., Ezeh, L. O. "Defect and doping concentration study with series and shunt resistance influence on graphene modified perovskite solar cell: A numerical investigation in SCAPS-1D framework", Journal of the Indian Chemical Society, 100(5), 101001, 2023. https://doi.org/10.1016/j.jics.2023.101001

[57] Dematage, N., Premalal, E. V. A., Konno, A. "Employment of CuI on Sb_2S_3 extremely thin absorber solar cell: N719 molecules as a dual role of a recombination blocking agent and an efficient hole shuttle", International Journal of Electrochemical Science, 9(4), pp. 1729–1737, 2014. https://doi.org/10.1016/S1452-3981(23)07886-0

[58] Noh, Y., Yoo, K., Kim, J.-Y., Song, O., Ko, M. J. "Iridium catalyst based counter electrodes for dye-sensitized solar cells", Current Applied Physics, 13(8), pp. 1620–1624, 2013. https://doi.org/10.1016/j.cap.2013.06.007

[59] Jahantigh, F., Safikhani, M. J. "The effect of HTM on the performance of solid-state dye-sanitized solar cells (SDSSCs): a SCAPS-1D simulation study", Applied Physics A, 125(4), 276, 2019. https://doi.org/10.1007/s00339-019-2582-0

[60] Obare, N., Isoe, W., Nalianya, A., Mageto, M., Odari, V. "Numerical study of copper antimony sulphide (CuSbS2) solar cell by SCAPS-1D", Heliyon, 10(5), e26896, 2024. https://doi.org/10.1016/j.heliyon.2024.e26896

[61] Wu, W.-Q., Wang, Q., Fang, Y., Shao, Y., Tang, S., …, Huang, J. "Molecular doping enabled scalable blading of efficient hole-transport-layer-free perovskite solar cells", Nature Communications, 9(1), 1625, 2018. https://doi.org/10.1038/s41467-018-04028-8

[62] Usman, A., Bovornratanaraks, T. "An extensive study of the impact of graphene passivation on HTLs (PTAA and NiO) in $MAPBI_3$ and $Cs_3Bi_2I_9$-based inverted perovskite solar cells for thermal stability in SCAPS 1D framework", Solar Energy, 284, 113043, 2024. https://doi.org/10.1016/j.solener.2024.113043

[63] Hossain, M. K., Datta, A. K., Alsalman, O., Uddin, M. S., Toki, G. F. I., Darwish, M. A., Mohammad, M. R., Dwivedi, D. K., Haldhar, R., Trukhanov, S. V. "An extensive study on charge transport layers to design and optimization of high-efficiency lead-free Cs_2PtI_6-based double-perovskite solar cells: A numerical simulation approach", Results in Physics, 61, 107751, 2024. https://doi.org/10.1016/j.rinp.2024.107751

[64] Ogunmoye, K. A., Izang, J. C., Olorunyolemi, I., Ozurumba, A. C., Danladi, E. "Highly efficient $MAGeI_3$ HTL-free perovskite solar cell with lithium-doped electron transport layer: A dive into SCAPS-1D simulation insight", Journal of Energy Technology and Environment, 7(2), pp. 34–50, 2025. https://doi.org/10.5281/zenodo.15598728

[65] Kharangarh, P., Misra, D., Georgiou, G. E., Chin, K. K. "Evaluation of Cu Back Contact Related Deep Defects in CdTe Solar Cells", ECS Journal of Solid State Science and Technology, 1(5), Q110, 2012. https://doi.org/10.1149/2.001206jss

[66] Kirchartz, T., Gong, W., Hawks, S. A., Agostinelli, T., MacKenzie, R. C. I., Yang, Y., Nelson, J. "Sensitivity of the Mott-Schottky analysis in organic solar cells", The Journal of Physical Chemistry C, 116(14), pp. 7672–7680, 2012. https://doi.org/10.1021/jp300397f

[67] Mao, L.-F. "Physical origin of the temperature-dependent open-circuit voltage in solar cells", Applied Physics A, 126(1), 42, 2020. https://doi.org/10.1007/s00339-019-3224-2